VILNIUS UNIVERSITY
CENTER FOR PHYSICAL SCIENCES AND TECHNOLOGY

Vytautas
JAKŠTAS

Compact Terahertz Emitters and Detectors Based on AlGaN/GaN Heterostructures

SUMMARY OF DOCTORAL DISSERTATION

Physical Sciences,
Physics 02 P

VILNIUS 2018

This dissertation was written between 2013 and 2017 at the Center for Physical Sciences and Technology.

Academic supervisor:
dr. Irmantas Kašalynas (Center for Physical Sciences and Technology, Physical Sciences, Physics – 02 P).

This doctoral dissertation will be defended in a public meeting of the Dissertation Defence Panel:

Chairman – prof. habil. dr. Jūras Banys (Vilnius University, Physical Sciences, Physics – 02 P).
Members:
dr. Grzegorz Cywiński (Institute of High Pressure Physics of the Polish Academy of Sciences, Physical Sciences, Physics – 02 P),
dr. Jan Devenson (Center for Physical Sciences and Technology, Physical Sciences, Physics – 02 P),
dr. Šarūnas Meškinis (Kaunas University of Technology, Technological Sciences, Material Engineering – 08 T),
prof. dr. Roland Tomašiūnas (Vilnius University, Technological Sciences, Material Engineering – 08 T).

The dissertation shall be defended at a public meeting of the Dissertation Defence Panel at 3 p. m. on 8th November, 2018 in auditorium A101 of the Center for Physical Sciences and Technology.

Address: Saulėtekio av. 3, LT-10257 Vilnius, Lithuania.

The text of this dissertation can be accessed at the libraries of the Center for Physical Sciences and Technology and Vilnius University as well as on the website of Vilnius University:
www.vu.lt/lt/naujienos/ivykiu-kalendorius.

VILNIAUS UNIVERSITETAS
FIZINIŲ IR TECHNOLOGIJOS MOKSLŲ CENTRAS

Vytautas
JAKŠTAS

Kompaktiški AlGaN/GaN heterosandūriniai terahercinės spinduliuotės šaltiniai ir jutikliai

DAKTARO DISERTACIJOS SANTRAUKA

Fiziniai mokslai,
fizika 02 P

VILNIUS 2018

Disertacija rengta 2013 – 2017 metais Fizinių ir technologijos mokslų centre.

Mokslinis vadovas:
dr. Irmantas Kašalynas (Fizinių ir technologijos mokslų centras, fiziniai mokslai, fizika – 02 P)

Gynimo taryba:
Pirmininkas – prof. habil. dr. Jūras Banys (Vilniaus universitetas, fiziniai mokslai, fizika – 02 P).
Nariai:
dr. Grzegorz Cywiński (Lenkijos mokslų akademijos Aukštų slėgių fizikos institutas (Instytut Wysokich Ciśnień, Polskiej Akademii Nauk), fiziniai mokslai, fizika – 02 P).,
dr. Jan Devenson (Fizinių ir technologijos mokslų centras, fiziniai mokslai, fizika – 02 P),
dr. Šarūnas Meškinis (Kauno technologijos universitetas, technologijos mokslai, medžiagų inžinerija – 08 T),
prof. dr. Roland Tomašiūnas (Vilniaus universitetas, technologijos mokslai, medžiagų inžinerija – 08 T).

Disertacija ginama viešame Gynimo tarybos posėdyje 2018 m. lapkričio mėn. 8 d. 15 val. Fizinių ir technologijos mokslų centro A101 auditorijoje.

Adresas: Saulėtekio al. 3, LT-10257 Vilnius, Lietuva.

Disertaciją galima peržiūrėti Fizinių ir technologijos mokslų centro bei Vilniaus universiteto bibliotekose ir Vilniaus universiteto interneto svetainėje adresu: www.vu.lt/naujienos/ivykiu-kalendorius.

SANTRAUKA

Terahercinio (THz) dažnio spinduliuote dažniausiai laikomi elektromagnetiniai virpesiai, kurių dažniai yra tarp 0,1 THz ir 15 THz (atitinkami bangos ilgiai tarp 3 mm ir 20 μm, o bangos skaičiai – maždaug tarp 3,3 cm^{-1} ir 500 cm^{-1}). Šis ruožas yra įsiterpęs tarp mikrobangų bei infraraudonųjų spindulių ir žymi ribą tarp klasikiniais krūvininkų pernašos dėsniais paremtos elektronikos bei kvantinės mechanikos principais aprašomos fotonikos [1]. Žvelgiant iš elektronikos pusės, THz dažnis yra per aukštas, kad krūvininkai spėtų į jį reaguoti. O žvelgiant iš fotonikos pusės, šis dažnis yra per žemas, kad būtų galima efektyviai valdyti elektronų perėjimus tarp lygmenų, ypač kambario temperatūroje. Taigi, kuriant THz dažnyje veikiančius prietaisus, tenka ieškoti netradicinių sprendimų, leidžiančių panaudoti tiek elektronikos, tiek ir fotonikos sričių privalumus.

THz spinduliuotės taikymai taip pat yra netradiciniai ir apima įvairias sritis: spektroskopiją, vaizdinimą, mikroskopiją, mediciną, kosmoso tyrinėjimus, saugumo sistemas, ryšius, metrologiją [2]. Dėl šių plačių THz spinduliuotės pritaikymo galimybių, plėtojasi medžiagų ir prietaisų tyrimai siekiant pagaminti kompaktiškus, kambario temperatūroje veikiančius, derinamo dažnio elektrinius plazmoninius THz spinduolius bei mechaniškai patvarius, paprastai gaminamus sparčius THz spinduliuotės jutiklius. Viena iš perspektyviausių medžiagų – tai IIIA grupės elementų nitridai, turintys unikalias fizines ir chemines savybes ir milžinišką potencialą elektronikos komponentų plėtros srityje.

Kompaktiškų ir efektyvių THz spinduliuotės šaltinių bei jutiklių kūrimo iššūkis kaip tik ir yra nagrinėjamas šiame darbe, kurio tikslas – iš AlGaN/GaN heterostruktūrų pagaminti didelio elektronų judrio tranzistorius bei „peteliškės“ tipo diodus ir ištirti jų tinkamumą THz spinduliuotei generuoti bei detektuoti.

Disertacija yra sudaryta iš įvado, šešių skyrių ir apibendrinimo. Įvade apibrėžiamas disertacijos temos aktualumas ir pagrindžiama

tiriamoji problema, pristatomas darbo tikslas ir uždaviniai bei naujumas, pateikti ginamieji disertacijos teiginiai, autoriaus indėlis bei publikacijų sąrašas. Pirmajame skyriuje apžvelgiami svarbiausi literatūros šaltiniai bei atlikti tyrimai disertacijos tema. Antrajame disertacijos skyriuje aprašoma bandinių gamybos technologija, o trečiajame – pagamintų bandinių charakterizavimas metodika bei rezultatai. Ketvirtajame skyriuje pateikiamas THz spinduliuotės detekcijos tyrimas panaudojant pagamintus elektronikos komponentus – HEMT ir „peteliškės“ tipo diodus. Penktasis skyrius yra skirtas spektriniams spinduliavimo iš THz spinduolių tyrimams, o paskutiniajame skyriuje pateikiama sekliųjų priemaišų elektroliuminescencijos analizė. Disertacijos pabaigoje apibendrinami gauti rezultatai ir išvados bei pateikiamas cituotos literatūros sąrašas.

INTRODUCTION

Electromagnetic waves with frequencies ranging from 0.1 THz to 15 THz (corresponding wavelengths from 3 mm to 20 μm and wavenumbers from approximately 3.3 cm^{-1} to 500 cm^{-1}) are most commonly considered as terahertz (THz) radiation. This range is sandwiched between microwaves and infrared rays and is considered to mark the boundary between electronics which is based on classical charge transport principles and photonics which is described by quantum mechanics [1]. Looking from the electronics side, the THz frequency is too high for the charges to respond; while looking from the photonics side, this frequency is too low to allow efficient control of electron transitions between energy levels, especially at room temperature. Therefore, the development of THz frequency devices requires unconventional solutions that would allow the use of both aspects – electronics and photonics.

Applications of THz radiation are also unconventional and cover various areas such as spectroscopy, imaging, microscopy, medicine, space exploration, security systems, communications, and metrology [2]. Due to wide possibilities of THz radiation application, a huge amount of effort is being put into research of materials suitable to develop and produce compact, frequency-tunable plasmonic THz emitters as well as mechanically durable, simply-manufactured, high-speed THz radiation sensors that should be capable of operating at room temperature. The IIIA group nitrides, which have unique physical and chemical properties as well as enormous potential for the development of electronic components, are considered to be among the most promising materials for the THz devices.

Main goal and objectives

The main goal of the dissertation is to develop high-electron mobility transistors (HEMTs) and bow-tie (BT) diodes from AlGaN/GaN heterostructures and investigate their availability for the emission and

detection of THz waves. In order to reach the goal, the following objectives were defined:

1. To optimize the procedures of ultraviolet photolithography for processing ohmic and Schottky contacts on AlGaN/GaN heterostructures grown by metalorganic chemical vapour deposition (MOCVD).
2. To design THz emitters based on high-electron mobility transistor (HEMT) with a large-area grating-gate electrode as well as bow-tie detectors, and to manufacture them from the AlGaN/GaN heterostructures.
3. To measure spectra of the THz emitters in frequency range from 1.5 THz to 13.5 THz (from 50 cm^{-1} to 450 cm^{-1}) at room and cryogenic temperatures and investigate the influence of the excitation method.
4. To evaluate the radiant flux of the THz emitters and assess the appropriateness to use them for the generation of THz radiation.
5. To evaluate performance of the AlGaN/GaN bow-tie diodes as well as high-electron mobility transistors that are not intentionally designed for usage as detectors.

Scientific novelty

- Technology for the processing of ohmic and Schottky contacts on AlGaN/GaN heterostructures has been developed and implemented in Lithuania (at the Center for Physical Sciences and Technology, FTMC).
- It has been shown that only two stages of standard ultraviolet (UV) photolithography are needed in order to shorten and cheapen the manufacture of the AlGaN/GaN Schottky diodes and high-electron mobility transistors. During these stages ohmic and Schottky contacts are produced. Electric parameters of components manufactured by the latter two-stage technology are comparable with the parameters of commercially available AlGaN/GaN components.

- Bow-tie (BT) diodes made of AlGaN/GaN heterostructures have been created for the THz detection. The sensitivity and noise equivalent power (*NEP*) of the BT diodes were up to 12 V/W and down to 0.45 nW√Hz, respectively, at 0.3 THz. The sensitivity of AlGaN/GaN BT diodes was comparable to that of InGaAs BT diodes which are the most sensitive at present, while the *NEP* was around ten times lower.
- AlGaN/GaN HEMTs were manufactured by using only two stages of ultraviolet photolithography. The sensitivity and noise equivalent power of the HEMTs were up to 2.6 V/W and 0.60 nW√Hz, respectively, at 0.3 THz.
- Calibrated spectral power distribution of emission from the AlGaN/GaN HEMT structure with large-area metal grating has been measured. The linewidth, quality factor, radiant flux, and radiant efficiency of ungated 2DEG plasmon emission peak have been determined from the spectra and yielded the values of about 52.5 cm^{-1}, 3.2, up to 940 nW, and up to $35 \cdot 10^{-9}$, respectively.
- It has been shown that in order to increase the radiant efficiency of THz emission which occurs due to plasmon decay in AlGaN/GaN HEMT structure with large-area metal grating, it is required (*i*) to cool the sample, (*ii*) to excite it by electric pulses of up to 0.1 W and 0.3 W for the samples grown on Al_2O_3 and SiC substrates, respectively, and (*iii*) to decrease the amount of residual silicon and oxygen impurities, which was of about 10^{17} cm^{-3} in the investigated samples.
- A possibility to investigate shallow impurities in the AlGaN/GaN heterostructures has been demonstrated by measuring electroluminescence spectra which originate due to electron transitions between energy levels of shallow impurities in the frequency range of 3 – 13.5 THz (100 – 450 cm^{-1}) at 110 K temperature.

Statements to defend

1. AlGaN/GaN Schottky diodes and high-electron mobility transistors with electrical parameters comparable to the commercial components can be manufactured by using only two stages of UV photolithography, during which ohmic and Schottky contacts are fabricated.
2. AlGaN/GaN heterojunction with two-dimensional electron gases is suitable for the manufacturing of sensitive THz-frequency detectors based on bow-tie diodes and high-electron mobility transistors.
3. Radiation of the electrically excited ungated plasmon in AlGaN/GaN heterojunctions with metallic grating-gate electrode is comparable or lower than thermal radiation of the sample and electroluminescence of shallow impurities.
4. Electroluminescence spectra in the THz frequency range allow investigating electron transitions in shallow impurities of AlGaN/GaN high-electron mobility transistor structures at 110 K temperature under short electric pulse excitation.

Contribution of the author

The author of the dissertation has designed photomasks for the UV photolithography and performed the majority of photolithography processes needed for the manufacturing of the samples. In addition, the author has made a significant contribution for the optimization of the spectrometer and performed most of the electric and spectral measurements. The author was also actively engaged in the preparation of the scientific papers and conference presentations related to the topic of the dissertation. Part of the latter has been presented personally by the author.

1. REVIEW

1.1. Properties of GaN

The very first scientific information about gallium nitride (GaN) reaches us from 1931 [3], however it has come in all the glory in 2014 due to the Nobel prize award for the invention of blue LED [4]. Gallium nitride has become so popular because of its superb physical properties, such as wide bandgap, high electron mobility, and perfect thermal stability [5]. Several figures of merit (FOM) have been created in order to compare semiconductors, e.g., Baliga FOM [6] or Johnson FOM [7]. According to them, GaN shows a better performance for the high power and high frequency applications as compared to that of traditional semiconductors such as Si or GaAs [5]. In addition, GaN has a very good chemical resistance [8]. Finally, it is worth saying that optical phonons in GaN appear in higher energies ($> 500\ cm^{-1}$) as compared to those in GaAs [9], [10], and this is very important for the manufacturing of THz range devices.

The substrate is one of the most important parts of any electronic device. The best quality of heterostructure is obtained if epitaxial layers (a.k.a. epilayers) are grown on the GaN (i.e., native) substrate. However, GaN substrates have appeared not long ago [11] and are still small in size and expensive. Due to the latter reasons nitride semiconductors are usually grown on Al_2O_3, Si or SiC substrates [12].

Growing on non-native substrates causes several shortages: heterostructures tend to bow [13], crack, and possess a lot of threading dislocations (TD) on the surface. All these effects are caused by the mismatch of lattice constant and coefficient of thermal expansion between the substrate and nitride epilayers. Dozens of methods have been developed in order to reduce TD density (TDD), e.g., growth of a thick GaN epitaxial layer [14], usage of vicinal substrates [15], insertion of a superlattice [16], application of the epitaxial lateral overgrowth technique [17], Si or Mg δ-doping [18] and many others.

Since nitrides are usually grown along the **c** axis, a huge intrinsic electric field (EF) appears due to spontaneous polarization [19]. Additionally, when the AlGaN/GaN heterostructure is grown, both piezoelectric polarization and additional EF appear due to the tensions originating from the different lattice constants in the epilayers [20]. These two effects cause formation of the two-dimensional electron gas (2DEG) near the AlGaN/GaN interface [19].

1.2. Plasmons in 2DEG

A plasmon is a quasiparticle, described as a rapid longitudinal oscillation of a charge density. In semiconductors, plasmons can be excited not only in volume but also in 2DEG. In general, the dispersion of 2DEG plasmons is described by equation [21]:

$$\omega_p = \sqrt{\frac{e^2 N_{2DEG}}{2m_e^* \varepsilon_0 \bar{\varepsilon}} k} \,. \tag{1.1}$$

Here e and m_e^* are the electron charge and effective mass, N_{2DEG} is the 2DEG density, ε_0 – the electric constant, $\bar{\varepsilon}$ – an effective dielectric function, and k – a plasmon wavenumber. The effective dielectric function depends on the composition of heterostructure. In case of a bare AlGaN/GaN heterostructure without metallisation (ungated case) [22],

$$\bar{\varepsilon}_u = \frac{1}{2}\left[\varepsilon_s + \varepsilon_b \frac{1 + \varepsilon_b \tanh\left(k_u w\right)}{\varepsilon_b + \tanh\left(k_u w\right)}\right]. \tag{1.2}$$

Here $\varepsilon_s = 9.5$ and ε_b are the dielectric constant of GaN and AlGaN, respectively, k_u – the wavenumber of ungated plasmon, and w – the thickness of the AlGaN layer. If the heterostructure is covered by a metal contact (gated case) [22]:

$$\bar{\varepsilon}_g = \frac{1}{2}\left[\varepsilon_s + \varepsilon_b \coth\left(k_g w\right)\right]. \tag{1.3}$$

Here k_g is the wavenumber of gated plasmon. Schematic view of gated and ungated 2DEG in AlGaN/GaN heterostructure is shown in Figure 1.

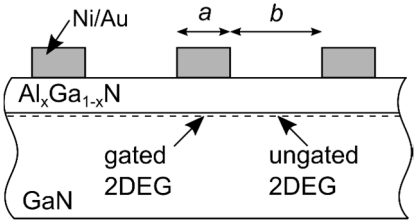

Figure 1. Cross-section schematic view of the AlGaN/GaN heterostructure partly covered with metal layer. *a* is a width of the metal stripe and *b* is a distant between adjacent stripes.

Plasmons in 2DEG can be excited in various ways, e.g. by irradiating with charged particles, applying an electric field or by a strong optical radiation [23]. However, the latter case can only be realized by covering the surface of semiconductor with a metal grating which couples the electromagnetic field with 2DEG [24] in order to preserve the quasi-impulse conservation law [25]. The same method is used to extract the electromagnetic waves from the plasmons in 2DEG to the free space [26]. The width of the metal stripe *a* and the distant between adjacent stripes *b* determine the wavenumber of gated and ungated plasmon, respectively [27]:

$$k_g = \frac{(2m-1)\pi}{a}, \qquad k_u = \frac{(2m-1)\pi}{b}. \tag{1.4}$$

Here *m* is a plasmon mode number.

THz emission of excited plasmons have been observed in Si MOS [28], AlGaAs/GaAs [26], [29], and InGaP/InGaAs/GaAs [30] heterostructures as well as in InGaAs [31], InAlAs [32], and AlGaN/GaN [33] HEMTs with nanometre-long channel. In all the experiments both the emitters and the detectors were cooled down to

liquid He temperature, and the measured radiant flux was in the range of several nW [34], [31]. It is obvious that low temperature and small radiant flux are the main shortages preventing a wide usage of such plasmonic THz emitters.

2. TECHNOLOGY OF SAMPLE MANUFACTURING

Lithuanian scientists have a long-lasting experience in semiconductor growth and investigation. However, most of the work have been done using Si, InGaAs and other narrowband semiconductors. Nitride metalorganic chemical vapour deposition (MOCVD) reactor had become available at Vilnius University in 2011, yet most research is done by contactless methods [35], [36]. It is obvious that for the manufacturing of electronic components and devices, technology of the processing of ohmic and Schottky contacts on nitrides must be implemented.

2.1. AlGaN/GaN Heterostructures

AlGaN/GaN heterostructures were grown on either sapphire or silicon carbide substrates by the MOCVD method at the Institute of Photonics and Nanotechnology of Faculty of Physics of Vilnius University (VU FF FNI), Lithuania (heterostructures VU393, VU394, and VU395) and at the Institute of High Pressure Physics (UNIPRESS), Poland (heterostructures TG2196, TG2219, and HX2688). The heterostructures consisted of high-resistivity GaN (HR-GaN) and low-temperature GaN (LT-GaN) buffers, followed by unintentionally-doped GaN (UID-GaN) layer, AlN spacer and undoped AlGaN barrier. An additional superlattice (SL) consisting of 20-nm-thick AlGaN/GaN layers was grown in the heterostructures VU394 and VU395. Parameters of the epilayers are summarised in Table 1.

The most important parameters which describe 2DEG are the density of two-dimensional electrons N_{2DEG} and their mobility μ. They are both determined by the AlGaN barrier thickness and by Al molar part in it. Surfaces of all the samples were examined by the atomic force microscope (AFM) and surface root mean square (RMS) roughness as well as TDD were calculated. The results are presented in Table 3 at the end of Chapter 3.

Table 1. Parameters of the epilayers in heterostructures.

Layer	TG2196	TG2219	VU393	VU394	VU395	HX2688
SiN_x	-	-	-	-	-	1 nm
GaN	-	-	-	-	-	2 nm
$Al_xGa_{1-x}N$	25 nm $x = 0.20$	27 nm $x = 0.23$	22 nm $x = 0.11$	18 nm $x = 0.26$	20 nm $x = 0.33$	19 nm $x = 0.25$
AlN	1 nm	1 nm	2 nm	2 nm	1 nm	1 nm
UID-GaN	500 nm	500 nm	n. d.	300 nm	300 nm	1000 nm
SL	-	-	-			-
HR-GaN LT-GaN	1000 nm	1000 nm	n. d.	n. d.	n. d.	n. d.
Substrate	Al_2O_3	Al_2O_3	Al_2O_3	Al_2O_3	Al_2O_3	SiC

n. d. – no data

2.2. UV Photolithography and Metal Contacts

A single stage of standard UV photolithography consists of the following steps:

1. Cleaning the surface;
2. Spin-coating and drying of photoresist;
3. Aligning and exposure;
4. Developing;
5. Certain process (e.g., mesa formation, metal evaporating, surface passivation, ion implantation, etc.);
6. Lift-off process;
7. Additional process on request (e.g., ohmic contact annealing, ion activation, etc.).

Usually one stage of photolithography is not enough to manufacture an electronic component. For instance, *Cree* uses at least seven lithography stages for their GaN HEMTs [37] while *Intel* needs more than 2000 lithography steps to make a processor of 14-nm

technology [38]. The second and any further stages are done similarly, except that the alignment step is needed. It requires the highest accurateness, however inaccuracies of up to 2 µm usually originate by using a standard UV photolithography.

Photomasks for the UV photolithography were designed by using open-source program KLayout and were manufactured at *Panevėžio mechatronikos centras* (Lithuania) and at *Compugraphics Jena GmbH* (Germany). In order to simplify the processing and make it convenient for fast prototyping, most of the designed components did not need a step of mesa formation. In such a case the processing becomes shorter, cheaper and the manufactured device contains less inaccuracies which emerge with the second and every further stages. Design of the components introduced in the dissertation is shown in Figure 2(a).

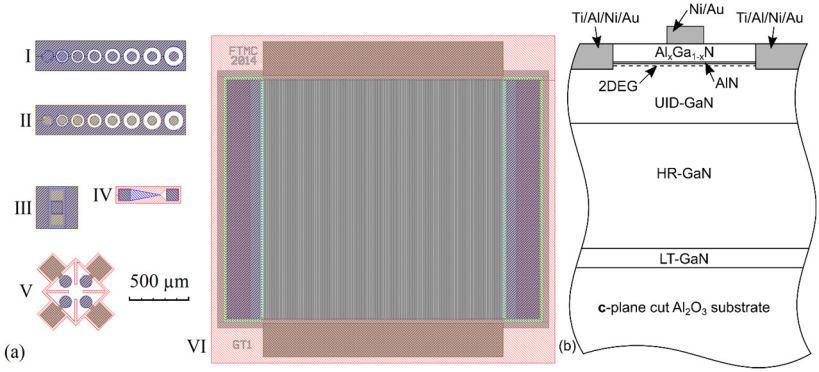

Figure 2. (a) Design of electronic components: I CTLM structure, II Schottky diodes, III HEMT, IV BT diode, V van der Pauw structure, VI large area HEMT with grating-gate electrode. (b) Cross-section schematic view of the AlGaN/GaN heterostructure with fabricated ohmic and Schottky contacts [P4].

Most of the samples were manufactured at the open-access centre at FTMC. The samples U31 and U33 were manufactured at UNIPRESS, but all the nanometre-width Schottky gratings were

manufactured at *Melbourne Centre for Nanofabrication* (Australia) by an electron-beam lithography.

Processing steps of the ohmic contact were as follows:

1. Cleaning the surface in "piranha" solution, deionised (DI) water and blowing in nitrogen gases.
2. Spin-coating and drying of the photoresist.
3. Exposure through a photomask by using *Karl Suss* MJB3 mask-aligner. A post-exposure bake and an additional full exposure is needed if an image-reversal photoresist is used.
4. Developing, DI rinsing and blowing in nitrogen gases.
5. Evaporating of Ti/Al/Ni/Au metal stack in high vacuum by using VST TFDS-870 electron-beam physical vapour deposition system.
6. Removing odd metal film from the sample.
7. Rapid thermal annealing (RTA) for 30 s at 830 °C in nitrogen ambient by using UNITEMP RTP-1300 oven.

Manufacturing procedures of the Schottky contact are almost the same, except that the metal stack of Ni/Au is evaporated without a need of RTA procedure. As it was mentioned, no mesa is needed for the operation of most of the designed components. Despite that fact, manufacturing processes at UNIPRESS involved inductively coupled plasma reactive ion etching (ICP-RIE) procedure [39]. However, the latter equipment is currently not available at FTMC, therefore laser ablation technique (available at the Department of Laser Technologies of FTMC) [40] was used to form the mesa for the sample U6. Cross-section schematic view of a typical sample is shown in Figure 2(b).

2.3. Samples

More than 100 samples containing more than 3000 various components have been manufactured in total during the PhD studies, including circular transmission line method (CTLM, Figure 3(a)) as well as van der Pauw test structures, Schottky diodes (SDs, Figure

3(b)), high-electron-mobility transistors (HEMTs, Figure 8), bow-tie (BT) diodes (Figure 11). Only a small amount of the samples are introduced in the dissertation and they are listed in Table 2. In addition, around 60 plasmonic THz emitters, i.e., large-area HEMTs with grating-type gate or source-drain electrodes (Figure 14) have been manufactured.

Table 2. Samples introduced in the dissertation.

Hetero-structure	Sample number	Research performed	Section
TG2196	#5, #3, #4	CTLM	3.1
	#6	CTLM, SD I-V & C-V, Hall effect, HEMT	3.1, 3.2, 3.3, 3.5
	U19 GT1, U19 GT8	THz emission	5.2, 5.3
	U11	THz emission	5.2, 5.3, 5.4
	U26	Electroluminescence of shallow impurities	6.1
TG2219	U8	SD I-V & C-V	3.2, 3.3
	U6	THz emission	5.2, 5.3
	U28	Electroluminescence of shallow impurities	6.1
VU393	VU12	Influence of SL: SD I-V & C-V, HEMT	3.4, 3.5
VU394	VU13		
	VU33	THz emission	5.2
VU395	VU31, VU32		
	VU14	Influence of SL: SD I-V & C-V, HEMT	3.4
HX2688	U37	SD I-V & C-V, Hall effect, HEMT	3.2, 3.3, 3.5
	U33	THz detection	4.1, 4.2
	U31	Electroluminescence of shallow impurities	6.2

2.4. Chapter Summary

In the second chapter of the dissertation the design of the electronic components has been shown and the technology of manufacturing has been described. It was noted that for the majority of components a photolithography step of mesa formation is not needed, allowing to simplify and shorten the manufacturing procedures. MOCVD-grown heterostructures were also introduced and their quality parameters were described. Finally, the list of the samples used in the dissertation was presented.

3. CHARACTERISATION OF THE SAMPLES

Before manufacturing electronic components, the RTA temperature of the ohmic contacts was optimized. Additionally, the ohmic and Schottky contacts were characterized by measuring current-voltage (I-V) and current-capacitance (C-V) characteristics of various electronic components. Measurements were performed by using *Cascade Microtech* EPS150TRIAX probe stationas well as *Keithley* 2400 and *Agilent* E3647A source-measurement units (for the I-V measurements) or *Agilent* 4294A precision impedance analyser (for the C-V measurements). All the measured data is summarised in Table 3 at the end of Chapter 3.

3.1. Ohmic Contacts

The performance of the ohmic contacts was optimized by using CTLM test structures [41]. The CTLM test structure consists of eight ohmic contact pads of diameter $2r$ = 80 µm surrounded by the ohmic contact area. The fabricated CTLM structure is shown in Figure 3(a). Both the circular inner and outer contacts were separated by a distance d varying from 5 µm to 40 µm. Contact resistance and specific contact resistivity were found from the dependence of normalized measured resistance R_T on distance d [42]:

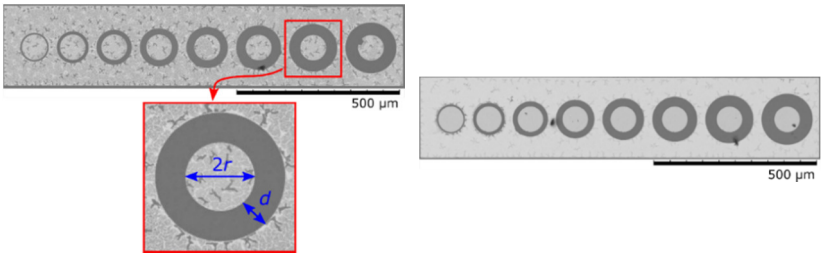

(a) (b)

Figure 3. Scanning electron microscopy (SEM) images of (a) CTLM test structure and (b) a series of Schottky diodes [P7].

$$R_T = \frac{R_{sh}}{2\pi r}\left(d + 2L_T\right)C\,, \tag{3.1}$$

$$L_T = \sqrt{\rho_c / R_{sh}}\,. \tag{3.2}$$

Here R_{sh} is a sheet resistance, L_T – a transfer length, and C – a correction factor.

The measured results are shown in Figure 4. The lowest contact resistance of R_c = 1.8 Ω·mm and specific contact resistivity of ρ_c = $3.4{\cdot}10^{-5}$ Ω·cm^2 was achieved at the RTA temperature of 830 °C. In addition, the transfer length of L_T = 1.9 µm and the sheet resistance of R_{sh} = 780 Ω/□ were obtained for the TG2196 heterostructure.

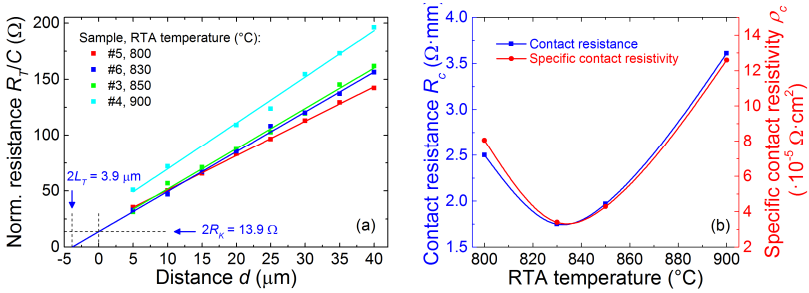

Figure 4. Investigation of the samples #5, #6, #3, and #4 annealed at various RTA temperatures: (a) the dependence of normalized resistance on the distance d of CTLM test structures and (b) calculated dependence of the contact resistance and the specific contact resistivity on the RTA temperature. Adapted from [P4] by adding the dependence of R_c on RTA temperature.

3.2. Schottky Contacts

The design of the Schottky diodes was similar to the CTLM test structure except that the Schottky contact was fabricated for the central contact (see Figure 3(b)). Direct current (DC) I-V characteristics of the samples U8, #6, and U37 SDs were measured at the applied voltage U ranging from -210 V to +2 V and are shown in Figure 5.

Even though the distance d between the electrodes of the SD differs 8 times, the mean value of the leakage current of the sample #6 was obtained of 49 ± 11 mA/cm^2 at the reverse voltage up to -210 V. As for the forward voltage, the maximum current of 360 A/cm^2 was reached for the diodes with d = 5 µm and was two times larger as compared to the SD with d = 40 µm. The leakage current was almost two orders of magnitude larger (3900 ± 500 mA/cm^2) in the sample U8 and that was attributed to the larger threading dislocation density (see Table 3). The performance of the sample U37 SDs showed much smaller leakage values around of 3.0 ± 1.2 mA/cm^2. Current switching ratio I_{ON}/I_{OFF} of the latter sample was of 50 dB in all the measured voltage range. In addition, none of the SDs underwent breakdown, representing a breakdown EF of SDs to be larger than 420 kV/cm for the sample U37.

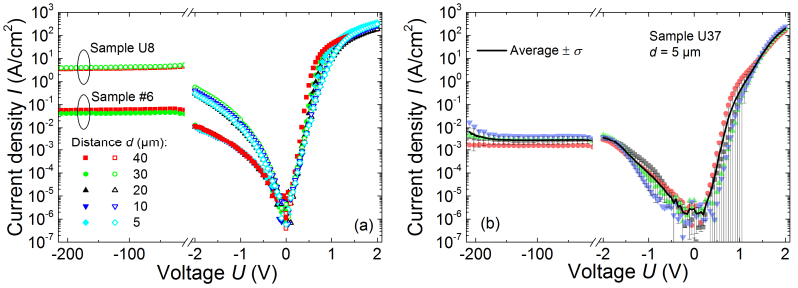

Figure 5. I-V characteristics of the Schottky diodes of the samples (a) U8, #6 (adapted from [P4] by adding characteristics of the sample U8), and (b) U37 [P1]. Here and further on the current I was normalized to the area of the Schottky contact $S_{SD} = \pi r^2 = 5.03 \cdot 10^{-5}$ cm^2.

The parameters of SDs grown on Al_2O_3 substrate were comparable with the results reported previously. For example, the leakage current ranged from about 1 A/cm^2 to 10 A/cm^2 at the reverse voltage of -10 V, and the forward current at +2 V was in the range of 100-1000 A/cm^2 [43]. As for the SDs on SiC substrate, the parameters were also similar [44] (leakage current of about 2-200 mA/cm^2

at -15 V, and forward current of about 100 A/cm^2 at +2 V), but felt behind the SDs on a bulk GaN substrate [43]. In the latter case, the leakage currents were up to one-hundredth in size.

3.3. Characterisation of 2DEG

Figure 6(a) shows the SD capacitance-voltage (C-V) characteristics measured at the applied bias voltage ranging from -7 V to 0 V. A threshold voltage U_{th} indicates a reverse bias voltage needed to fully deplete and close the conductive 2DEG channel. In our experiments different U_{th} values were measured independently of the modulation frequency in the samples U8, #6, and U37. The 2DEG density N_{2DEG} was evaluated by using an integral capacitance technique [42]:

$$N_{2DEG} = \frac{1}{eS}\int_{U_{th}}^{0} C_P(U)\,dU\ . \tag{3.3}$$

Here e is the electron charge and $C_P(U)$ is the measured dependence of capacitance on the reverse voltage bias. The calculated values for the samples U8, #6, and U37, were of $(8.6 \pm 0.5)\cdot 10^{12}$ cm^{-2}, $(5.0 \pm 0.1)\cdot 10^{12}$ cm^{-2}, and $(5.9 \pm 0.1)\cdot 10^{12}$ cm^{-2}, respectively.

The dependence of the carrier density on the depth is presented in Figure 6(b). The depth W and the carrier density N_a were calculated at

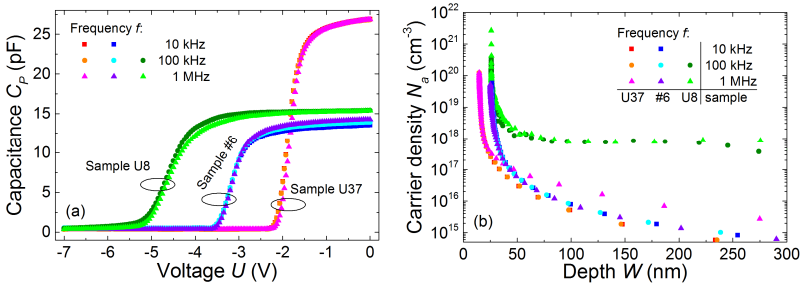

Figure 6. (a) C-V characteristics of the SDs with d = 40 µm of the samples U8, #6, and U37 at selected modulation frequency. (b) Charge distribution along the AlGaN/GaN interface calculated from the C-V characteristics by using Equations (3.4) and (3.5) [P1], [P4].

each point of the measured C-V characteristic by formulae [42]:

$$W = \frac{\varepsilon\varepsilon_0 S}{C_P}, \tag{3.4}$$

$$N_a = -\frac{C_P^3}{e\varepsilon\varepsilon_0 S^2 \, dC_P(U)/dU} \tag{3.5}$$

Here $\varepsilon = 8.9$ is the relative permittivity of GaN, ε_0 is the electric constant, and $dC_P(U)/dU$ is the first order derivative of $C_P(U)$. The position of the 2DEG was found to be at 27 ± 2 nm, 26 ± 0 nm, and 15 ± 0 nm from the surface for the samples U8, #6, and U37, respectively, and is in agreement with the barrier thickness determined from the X-ray diffraction measurement.

The 2DEG mobility was calculated by using the following equation [42]:

$$\mu = \frac{1}{eN_{2DEG}R_{sh}} \tag{3.6}$$

Here N_{2DEG} is the 2DEG density calculated from the C-V characteristics and R_{sh} is the sheet density calculated from the CTLM measurements. Calculated values for the samples U8, #6, and U37 were of 1650 $cm^2/(Vs)$, 1400 $cm^2/(Vs)$, and 1820 $cm^2/(Vs)$, respectively.

The 2DEG density and the mobility have been also determined by means of Hall effect measurement. The values of $9.2 \cdot 10^{12}$ cm^{-2} and 1340 cm^2/Vs were obtained for the TG2196 heterostructure (sample #6) as well as of $8.3 \cdot 10^{12}$ cm^{-2} and 1880 cm^2/Vs for the HX2688 heterostructure (sample U37) at room temperature (RT). Note that the 2DEG density obtained from the Hall experiment is up to two times larger as compared with the value calculated from the C-V measurements. The difference is caused by an unequal condition of the 2DEG during the measurements. In case of C-V measurement the heterostructure is covered by the Schottky contact which shallows the quantum well and lowers the 2DEG density. No such effect occurs during the Hall effect measurement. Different 2DEG density affects the frequency of plasmons in gated and ungated regions of

heterostructure and therefore should be accounted during the calculations done by Equation (1.1). Nevertheless, the calculated and measured 2DEG mobility was similar when both methods were applied, indicating that CTLM I-V and Schottky diode C-V measurement can serve as an alternative for the 2DEG mobility evaluation.

3.4. Influence of a Superlattice

It has been demonstrated that the insertion of a superlattice (SL) into a heterostructure reduces threading dislocation density (TDD) in the upper AlGaN epilayer [16]. In addition, a content of AlN in AlN/GaN SL has also been found to be essential for the growth of high quality heterostructures [45]. In the majority of cases structural analysis such as an X-ray diffraction (XRD) and various microscopy techniques are used to inspect and evaluate the fabricated heterostructures. However, less studies are oriented towards direct evaluation of the electronic devices performance, especially of those with the SL, e.g., laser diodes [46], HEMTs [47], and UV detectors [48].

Therefore, there is a need of experimental data to understand the impact of SL on the electrical performance of GaN-based electronic devices. I-V characteristics of the Schottky diodes made of heterostructures with SL (VU394 and VU395) and without SL (VU393) are shown in Figure 7(a). The performance of the SDs in the forward voltage range was similar to those of the samples U8 and #6: the current started to saturate at around +1 V and the maximum current up to 600 A/cm^2 was reached in various samples (see Table 3 for details). As for the reverse voltage, two regions can be distinguished. Rapid increase of leakage current was seen up to reverse voltage of -15 V and a slower increase afterwards. This phenomenon was attributed to different nature of leakage current – a surface leakage dominates at relatively small negative voltage values, while the leakage in volume (e.g., between GaN buffer and SL) originates at higher negative voltages [49].

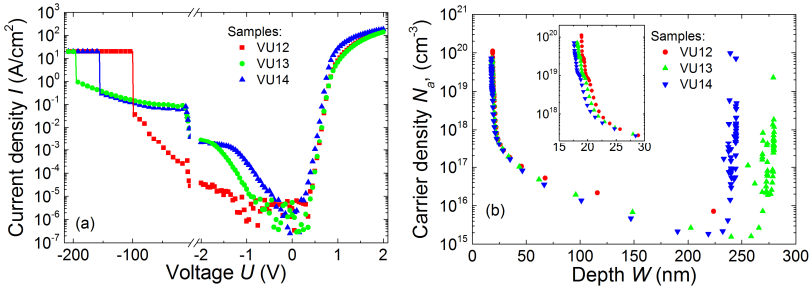

Figure 7. SD performance of the samples VU12, VU13, and VU14: (a) I-V characteristics and (b) charge distribution along the AlGaN/GaN interface calculated from the C-V characteristics by using Equations (3.4) and (3.5). Inset shows the same characteristics in a narrower range of depth *W*.

Higher leakage currents were obtained in the samples with SL (VU13 and VU14) as compared with the sample without SL (VU12) and this was attributes to higher TDD and surface RMS roughness of the former samples (see Table 3). Nevertheless, the SDs breakdown EF in the samples with SL was higher, i.e., 57 ± 9 kV/cm and 52 ± 10 kV/cm in the samples VU13 and VU14, respectively, as compared with the value of 40 ± 15 kV/cm in the sample without SL (VU12). This result shows that the breakdown occurs not in the surface but in the volume, most probably – in the interface of SL, in accordance with increasing leakage currents.

Charge distribution along the AlGaN/GaN interface of the samples VU12, VU13, and VU14 were also calculated from the C-V characteristics and are shown in Figure 7(b). An increase of the charge density can be clearly seen in the depth of approx. 240-280 nm of the samples VU13 and VU13 indicating a parasitic conduction channel formed in the vicinity of the GaN-SL interface. This additional conduction channel influences the electrical performance of the electronic components, e.g., causes lower sheet density and higher leakage current.

3.5. High-Electron-Mobility Transistors

The design of the manufactured high-electron-mobility transistor (HEMT) is shown in Figure 8. The HEMT consists of a rectangular drain in the centre surrounded with a ring-shape double-gate and with a ring-shape source electrode. The size of the gate is $L_G \times L_W =$ 5.5×100 µm with the spacing between source-drain and drain-gate of L_{SD} = 11.5 µm and L_{DG} = 2.0 µm, respectively.

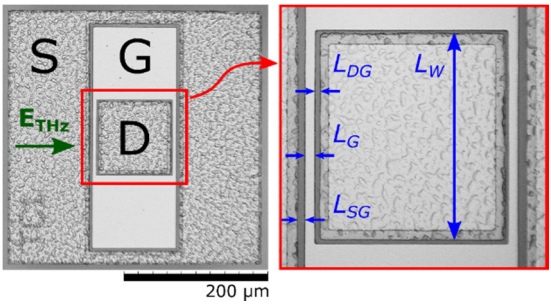

Figure 8. Photo of a high-electron-mobility transistor. Letters S, D, and G denote source, drain, and gate electrodes, respectively [P1].

The DC-output characteristics of the manufactured HEMT in the samples #6, VU12, VU13, and U37 are shown in α part of Figure 9. The maximum drain saturation current and the smallest ON-state resistance (R_{ON}) were obtained in the sample U37 and were of 450 mA/mm and 39 Ω, respectively. Lower drain saturation currents of 320 mA/mm, 190 mA/mm, and 300 mA/mm were obtained for the samples #6, VU12, and VU13, respectively. The channel of the latter sample was not closed even at U_{GS} = -3 V due to additional conduction channel near the GaN-SL interface. It is also worth noting that only sample U37 demonstrated almost no decrease of the current in the high U_{DS} region indicating much more efficient Joule heat dissipation due to ten times higher thermal conductivity of the SiC as compared to that of the sapphire.

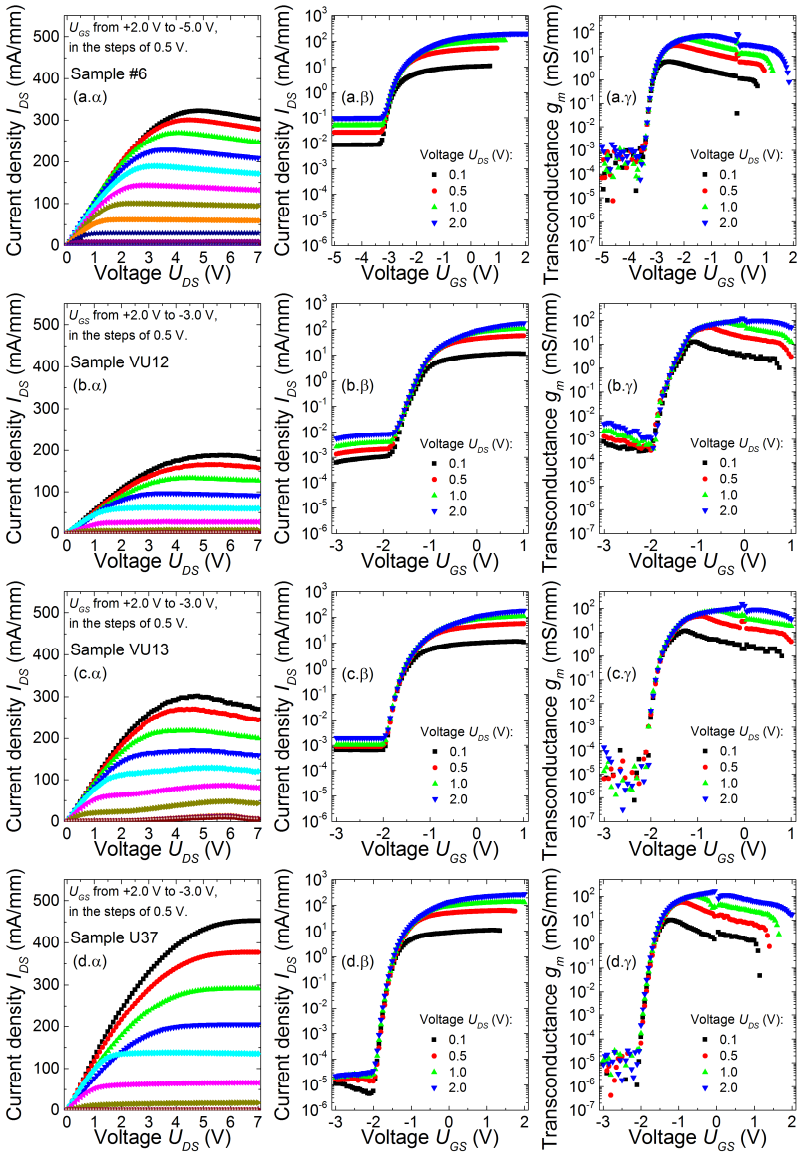

Figure 9. Measured DC characteristics of HEMTs of the samples #6 [P4], VU12 [P7], VU13 [P7], and U37 [P1]: (α) output at the gate voltage from +2.0 V to -3.0 V, (β) transfer and (γ) transconductance at selected drain values. The current I_{DS} in (α) and (β) parts was normalised to the double width of HEMT gate, $2L_W = 200$ µm.

The DC-transfer characteristics are shown in β part of Figure 9. The threshold voltage in different samples was consistent with the value obtained from C-V measurements (see Figure 6 and Table 3). HEMT of the sample U37 demonstrated the best electrical parameters among the samples tested, i.e., leakage current weakly depended on the U_{GS} voltage and was itself the smallest. Therefore, the current ON-OFF ratio was up to $I_{ON}/I_{OFF} = 1.2 \cdot 10^7$, that is at least 100 times larger as compared to that of any other sample. Calculated transconductance characteristics are shown in γ part of Figure 9. The largest transconductance at $U_{DS} = +2$ V and $U_{GS} = 0$ V was obtained in the sample U37 and had a value of $g_m = 170$ mS/mm.

Electrical parameters of the commercially available HEMTs on SiC [37] and on bulk GaN [50] substrates only slightly exceed the parameters of HEMT on SiC shown in this section. The largest saturated current mentioned in the literature reaches 1-1.2 A/mm, while transconductance is up to 220-360 mS/mm. It should not be forgotten that in this work only two stages of standard UV photolithography were used. Additional stages could further improve electrical parameters, e.g., surface passivation would reduce leakage currents.

3.6. Chapter Summary

Methods of sample characterisation have been described and the results have been introduced in the third chapter of the dissertation. At first, optimisation of the ohmic contact by CTLM measurement was demonstrated. Next, the performance of the Schottky contacts was investigated by measuring I-V and C-V characteristics of the Schottky diodes. Properties of 2DEG were determined in two ways: by the Hall effect measurement and by the C-V measurements of the Schottky diodes. An influence of the superlattice on the electrical properties was also analysed. Finally, electrical parameters of HEMTs manufactured from various heterostructures were demonstrated and compared.

Table 3. Summarized parameters of heterostructures, CTLM structures, Schottky diodes and high-electron mobility transistors. D_{dis} (TDD) and R_a (surface RMS roughness) were obtained from the AFM measurements; W_{2DEG} (2DEG depth), U_{th} (threshold voltage), and N_{2DEG} (2DEG density of gated electrons) were obtained from the SD C-V measurements when f = 100 kHz; R_{sh} (sheet density) was obtained from the CTLM measurements; μ (carrier mobility) was obtained from the Hall effect measurements at RT; I_{leak} (leakage current density when U = -10 V), I_{MAX} (forward current density when U = +2 V), and E_b (breakdown EF) were obtained from the SD I-V measurements; R_{ON} (resistance of open channel), I_{ON}/I_{OFF} (on-to-off current ratio), and g_m (transconductance when U_{DS} = +2 V) were obtained from the HEMT I-V measurements.

Hetero-structure	D_{dis} cm^{-2}	R_a nm	W_{2DEG} nm	U_{th} V	N_{2DEG} $\cdot 10^{12}$ cm^{-2}	R_{sh} Ω/□	μ $cm^2/(V \cdot s)$	I_{leak} mA/cm^2	I_{MAX} A/cm^2	E_b kV/cm	R_{ON} Ω	I_{ON}/I_{OFF} $\cdot 10^6$	g_m mS/mm
TG2196	$2.0 \cdot 10^9$	0.62	26 ± 0	-3.4	5.0 ± 0.1	780	1340	49 ± 11	360	> 70	45	0.0021	80
TG2219	n. d.	0.96	27 ± 2	-5.2	8.6 ± 0.5	440	n. d.	3900 ± 500	310	> 70	n. d.	n. d.	n. d.
VU393	$1.1 \cdot 10^9$	0.40	19 ± 0	-1.8	4.0 ± 0.0	670	n. d.	0.4 ± 0.1	400	40 ±15	85	0.032	120
VU394	$3.4 \cdot 10^9$	0.60	19 ± 0	-2.0	4.7 ± 0.0	620	n. d.	58 ± 6	310	57 ± 9	49	0.10	150
VU395	$3.9 \cdot 10^9$	0.88	18 ± 0	-1.5	3.6 ± 0.0	860	n. d.	72 ± 11	610	52 ± 10	n. d.	n. d.	n. d.
HX2688	n. d.	0.44	15 ± 0	-2.1	5.9 ± 0.1	600	1880	3.3 ± 1.1	198	> 420	39	12	170

n. d. – no data

4. THZ DETECTION

The main parameters describing different detectors are sensitivity J and noise equivalent power (NEP). After performing a raster scan of an incident THz beam, the sensitivity is calculated by [51]:

$$J = \frac{\pi}{\sqrt{2}} \frac{\int U_d \mathrm{d}S_p}{P_{spind} S_d}. \tag{4.1}$$

Here U_d is a lock-in signal of a detector, $\mathrm{d}S_p$ – an area of a raster point, P_{spind} – radiant flux of incident beam, and $S_d = \lambda^2/4\pi$ is an area of the isotropic antenna. NEP is calculated as follows [51]:

$$NEP = \frac{\sqrt{4k_B TR}}{J}. \tag{4.2}$$

Here T is temperature of the detector and R – detector's resistance.

4.1. Detection with HEMT

Operation of a field-effect transistor (FET) detector is based on the rectification of plasma waves in a 2DEG channel [52]. As plasma waves can also emerge in a HEMT channel, it is worth to examine a possibility to detect THz waves using the HEMT that was described in the previous chapter. A HEMT of the sample U33 with similar electrical characteristics as shown in Figure 9(d) was chosen for the investigation.

Optical set-up of the experiment is shown in Figure 10(a). A commercial VDI AMC364 electronic frequency multiplier chain (radiant flux of up to 11 mW) was used as a 0.3 THz frequency radiation source. Radiant flux was electrically modulated at 1 kHz and detected by a lock-in amplifier technique. The THz beam was focused into the HEMT from the substrate side by using an off-axis parabolic (OAP) mirror OAPV2 (diameter 5 cm, focal length F = 10 cm) and an aplanatic silicon lens AM. The orientation of the incident THz EF with respect to HEMT electrodes is shown in Figure 8.

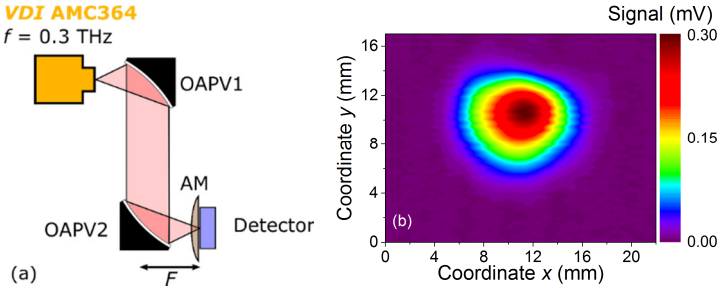

Figure 10. (a) Optical set-up of THz detection. (b) Beam profile of a 0.3 THz frequency source measured by using HEMT of the sample U33 at U_{GS} = 0 V. Area of raster point is S_p = 0.3 × 0.3 mm^2 here and further on [P1].

The HEMT was connected in a common-source mode circuit, positioned on translation stage and raster scanned in the focal plane of the focused THz beam. The result is presented in Figure 10(b). Sensitivity J and noise equivalent power NEP were estimated by Equations (4.1) and (4.2). In the case of U_{GS} = 0 V, the HEMT demonstrated values of J = 2.6 mV/W and NEP = 0.60 nW/√Hz, while at U_{GS} = -1.5 V, these values were of J = 7.5 V/W and NEP = 2.7 nW/√Hz, respectively.

4.2. Detection with BT Diodes

In order to compare the THz detection results, the same profiling was performed by using BT diodes of the same sample U33. A photo of such BT diodes and the orientation of the THz EF is shown in Figure 11. A BT diode consists of an asymmetrically shaped AlGaN/GaN structure with one pointed side metallized. An idea of a BT diode was firstly announced in 1994 and its operation is based on a non-uniform heating of 2DEG [53].

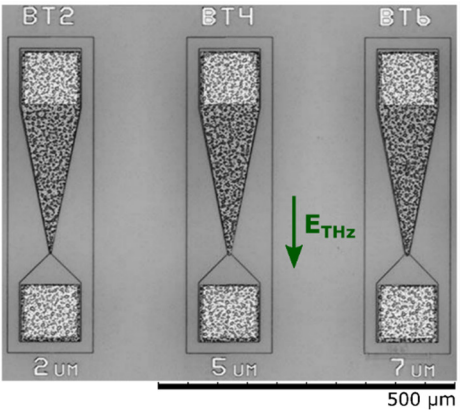

Figure 11. Photo of BT diodes with different apex width of 2 µm, 5 µm, and 7 µm [P5].

Figure 12(a) depicts asymmetry coefficients calculated as $A = (I_F\text{-}I_B)/(I_F+I_B)$ [54] of the BT diodes with different apex. Here I_F and I_B are the forward and the backward current at selected applied voltage, respectively. The largest asymmetry was obtained for the BT diodes with the smallest apex.

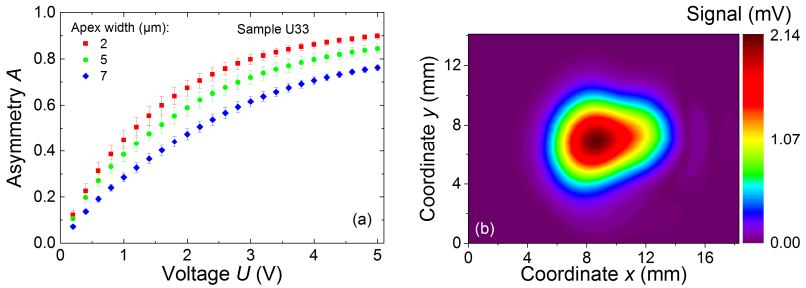

Figure 12. (a) Dependence of current asymmetry coefficients on applied voltage of the BT diodes with various apex width [P5]. (b) Beam profile of a 0.3 THz frequency source measured by using a BT diode with 7-µm-width apex of the sample U33.

Beam profile of the focused THz beam measured using BT diode with 7-µm-width apex is shown in Figure 12(b). No voltage was

applied to the BT diode during the measurement. Sensitivity J and NEP calculated by Equations (4.1) and (4.2) were of $J = 12$ V/W and $NEP = 0.45$ nW/√Hz, respectively. As for the BT diodes with smaller apex, the values were of $J = 7.5$ V/W and $NEP = 0.81$ nW/√Hz (5-µm-width apex), as well as of $J = 4.1$ V/W and $NEP = 1.8$ nW/√Hz (2-µm-width apex). Contrary to expected from the asymmetry calculation, BT diodes with smaller apex showed worse results and this can be explained by the fact, that no DC voltage was applied to the BT diode during the measurement [54].

Both the AlGaN/GaN HEMT (operating in a detector mode) and the BT diode showed similar sensitivity as InGaAs BT diodes (10 V/W) [54] and at least ten times higher sensitivity than GaAs BT diode (0.3 V/W) [55]. NEP was one-tenth in size as of InGaAs BT diodes (5.8 nW/√Hz) [54] or AlGaN/GaN HEMT with 250-nm-width gate contact (5 nW/√Hz) [56]. NEP of both the detectors described in this chapter was approximately ten times larger as compared to the FET detectors which have optimized antennas for the THz detection (TeraFET, 42 nW/√Hz) [57].

4.3. Chapter Summary

This chapter have been assigned for the investigation of THz detection. Imaging of the commercial THz source was performed by using manufactured BT diodes and HEMT which was not intentionally designed for the usage as a detector. Finally, the parameters of the detectors were calculated and compared.

5. THZ EMISSION FROM HEMT WITH LARGE-AREA METAL GRATING

Three methods corresponding to distinct states of 2DEG were used to excite the THz emission in the sample. Initially, the sample was externally heated without applying a voltage and the thermal emission spectra were measured. Then, direct current was applied through the channel of the sample. Finally, the sample was driven by the voltage pulses at a frequency of 12.5 Hz and a duty cycle (*DU*) varying from 0.5% to 50% (corresponding to the duration of pulses τ_p from 0.4 ms to 40 ms). Emission spectra were measured at room and cryogenic temperature of 110 K. Voltage pulses were generated by *Keysight* B2901A source-meter unit while the spectra were measured in vacuum by using a modified Fourier-transform infrared (FTIR) spectrometer.

5.1. Experimental Set-up and Black Body Radiation Model

Optical set-up of the modified LAFS-1000 spectrometer is shown in Figure 13(a). The radiated flux is collimated by an OAP mirror OAPV and diverted to a Michelson interferometer consisting of a moving mirror V2, a stationary mirror V3, and a 6-µm-thick polyethylene beam splitter BS. A focused beam is then detected with an optoacoustic detector (Golay cell) by using a lock-in amplifier technique at a frequency of 12.5 Hz. The sensitivity of Golay cell is flat over a very broad range of frequencies and has a value of $J = 10^4$ V/W and the $NEP = 10$ nW/√Hz [58]. A spectrum is obtained by measuring an interferogram and performing a fast Fourier transform (FFT). Spectral resolution is defined by the distance travelled by mirror V2 and was up to 2.0 cm^{-1} during the experiments. The spectral range is defined by the thickness of BS used [59]. In a case of 6-µm-thick BS, the spectral range was from 50 cm^{-1} to 450 cm^{-1}. An opto-mechanical modulator OM was used only when the sample was excited thermally or by DC voltage.

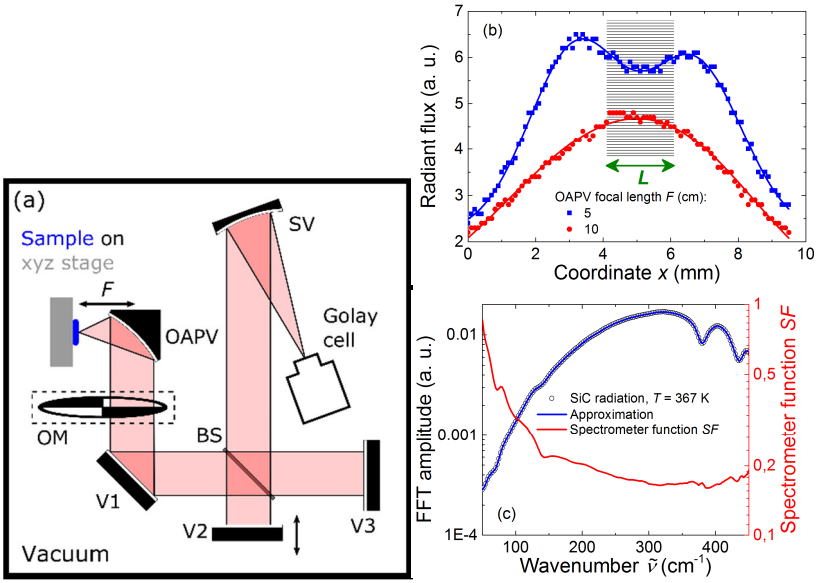

Figure 13. (a) Optical set-up of vacuumed FTIR spectrometer. (b) Dependence of radiant flux on coordinate x when OAP mirrors with different focal length are used. (c) Radiation spectrum of thermally excited SiC crystal fitted by Equation (5.1) and a spectrometer function $SF(\tilde{\nu})$.

The sample was mounted on the cold finger of a liquid-nitrogen cryostat-heater allowing to stabilize the temperature of the sample from 88 K to 400 K. The cryostat was mounted on a 3-axis translation stage for accurate positioning. In order to make sure the emission is collected solely from the region with a grating, a scan through the sample in both x and y directions was performed by moving the sample and registering the radiant flux. Figure 13(b) shows a comparison of the scans when OAP mirrors with different focal length are used. In case of 5 cm focal length OAP mirror, a double-hump-shaped curve was observed. Since the grating region is partly covered by a metallic contact, it reflects a part of the emission back to the heterostructure, simultaneously reducing the amount of flux emitted to the open space.

Taking this into account, the dip in the latter curve clearly shows the exact place of the grating. Since the length and width of the grating is $L = 2$ mm, a rough evaluation gave the size of the spot diameter of $D \approx 1.5$ mm $< L$ proving that the emission was collected purely from the area with the grating. If 10 cm focal length OAP mirror is used, a single-hump-shape curve is seen meaning that the radiation was also collected from the regions outside of the grating. In this case it is neither possible to evaluate the spot diameter nor the exact position of the grating.

Before measuring spectra of the samples, FTIR spectrometer was calibrated by using a thermal emission of n-type 4H-SiC crystal. Considering the latter as a black body (BB) [60], the measured spectrum can be described as follows [59]:

$$\begin{aligned} I_{SiC}\left(\tilde{\nu},T\right) &= SF\left(\tilde{\nu}\right)\times\left[1-R_{SiC}\left(\tilde{\nu}\right)\right]\times \\ &\times T_{BS}\left(\tilde{\nu}\right)\times R_{BS}\left(\tilde{\nu}\right)\times\left[B_e\left(\tilde{\nu},T\right)-B_e\left(\tilde{\nu},T_0\right)\right] \end{aligned}. \tag{5.1}$$

Here $SF\left(\tilde{\nu}\right)$ is a calibration function of the spectrometer, $R_{SiC}\left(\tilde{\nu}\right)$ – a reflectance function of SiC, $T_{BS}\left(\tilde{\nu}\right)$ and $R_{BS}\left(\tilde{\nu}\right)$ – transmittance and reflectance functions of BS, while $B_e\left(\tilde{\nu},T\right)$ and $B_e\left(\tilde{\nu},T_0\right)$ denote spectral radiance of BB at temperatures T and T_0, respectively, described by Plank's law. Functions $R_{SiC}\left(\tilde{\nu}\right)$, $T_{BS}\left(\tilde{\nu}\right)$, and $R_{BS}\left(\tilde{\nu}\right)$ were measured experimentally.

Emission spectrum of SiC crystal was measured at $T = 367$ K and is shown in Figure 13(c). Calibration function $SF\left(\tilde{\nu}\right)$ was determined by fitting the experimental SiC spectra with Equation (5.1). Therefore, the experimental spectrum of SiC crystal and the spectrometer calibration function were used to recalculate FFT amplitude from arbitrary units of measurement to spectral flux units (W/THz) by an equation deduced from (5.1):

$$\Phi_{e,\nu} = \frac{1}{c}\int \mathrm{d}\Omega \int \mathrm{d}S_{\Phi}\, \frac{B_e\left(\tilde{\nu},T\right)-B_e\left(\tilde{\nu},T_0\right)}{I_{SiC}\left(\tilde{\nu},T\right)} \tag{5.2}$$

Here $S_{\Phi} = 0,25\pi D^2$ is the area of the sample, from which the emission is collected.

5.2. Plasmonic Emitters

A HEMT with a large-area metal-grating is called a plasmonic emitter. Metal grating is used to extract the energy of plasmons excited in 2DEG channel. The energy is released to the open space in form of electromagnetic waves in THz frequency range [61].

The samples U19 and U11 made of TG2196 heterostructure and the sample U6 made of TG2219 heterostructure were chosen for the investigation of plasmonic emission. An active area of all the samples was of $L \times L = 2 \times 2$ mm^2. Ohmic contacts were manufactured along the grating stripes allowing to apply an electric current. Plasmonic samples were distinguished by the grating type (ohmic or Schottky) and the width and period of the stripes. Four samples have been chosen for the investigation of plasmonic radiation and parameters of theirs grating are presented in

Table 4. The active area of the sample U19 GT1 consisted of Schottky grating having the stripes width of $a = 4$ μm and the gap between the adjacent stripes of $b = 3$ μm. Grating of the sample U19 GT8 had the same measurements, but the grating consisted of grating-drain and grating-drain electrodes. Nanometre- width grating was manufactures for the samples U11 and U6. In addition, the latter

Table 4. Grating parameters of the THz emitters.

Sample	Grating type	a, nm	b, nm	g	P, nm	FF
U19 GT1	Schottky	4000	3000	1	7000	0.57
U19 GT8	ohmic	4000	3000	1	7000	0.57
U11	Schottky	370	665	1	1035	0.36
U6	Schottky	120	80	20	7000	0.34

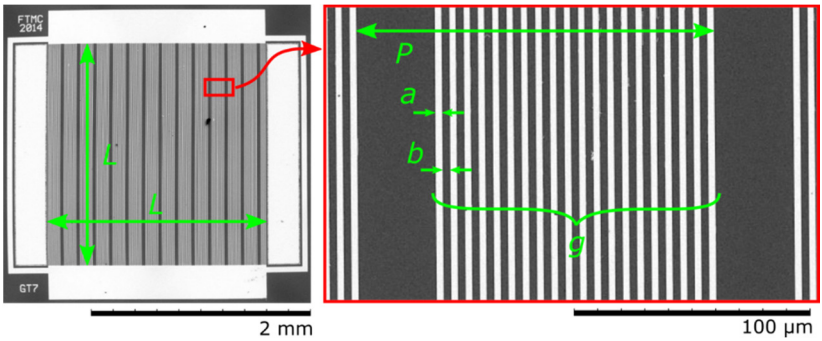

Figure 14. SEM image of the sample VU33 GT7 at different zoom. Parameters of the grating are as follows: a denotes the width of the metal stripe, b – the gap between adjacent stripes, and g – the number of stripes within the period P.

sample was designed with double periodicity, i.e., stripes were grouped in number of g having a group period of P. SEM image of such a sample is shown in Figure 14. A filling factor, i.e., a part of active area covered by the metal, was calculated as $FF = a \times g/P$.

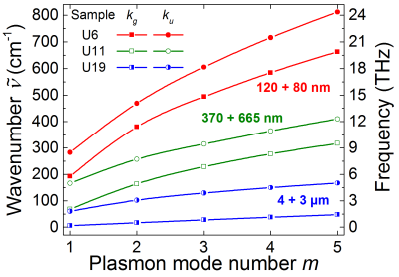

Figure 15. Modes of gated (k_g) and ungated (k_u) plasmons of the samples U6, U11, and U19 calculated by Equation (1.1).

Figure 15 depicts the dispersion of the plasmons calculated by Equation (1.1) that can be excited in the samples U19 GT1, U19 GT8, U11, and U6. The fundamental plasmon modes has the highest probability to be observed. In the sample U19 these modes lie in the

frequency range up to 100 cm^{-1}. By narrowing the stripes and the gap between them (samples U6 and U11) the fundamental and higher plasmon modes are pushed into a higher frequency range.

5.3. Radiation of Thermally Excited Plasmonic Emitters

Experimental data of thermally stimulated THz emission spectra of the samples U19 GT1, U19 GT8, U11, U6 and a TG2196 heterostructure without metallization (reference) are shown in Figure 16(a). Thermally stimulated emission spectrum of TG2196 heterostructure was fitted by Equation (5.1) and hence is precisely described by the BB radiation in a broad range of frequencies. As for the samples with grating-electrodes small deviations from the theoretical model can be seen indicating the influence of grating to the emission spectrum. The largest discrepancy can be seen in the frequency range from 50 cm^{-1} to 200 cm^{-1} of the sample U19 GT8 and was attributed to a higher roughness of the ohmic grating as compared to the Schottky grating in other samples.

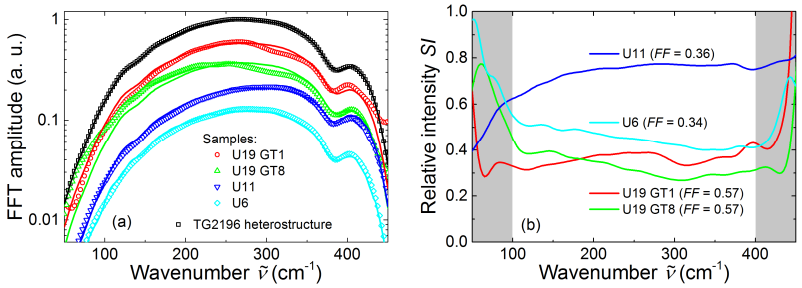

Figure 16. Measured (points) and fitted (line) emission spectra of the thermally excited TG2196 heterostructure and the samples U19 GT1, U19 GT8, U11, and U6. The measured spectra were shifted vertically by a factor of 0.6. (b) Relative radiation intensity of the same samples.

In order to get a stronger evidence on the influence of grating to the spectra, relative radiation intensity of the samples was calculated

as $SI = I_{sample}/I_{heterostructure}$. Here I_{sample} is spectrum of the sample and $I_{heterostructure}$ is spectrum of the respective heterostructure without metallisation. As it is seen in Figure 16(b), the samples U19 GT1 and U19 GT8 were distinguished by a much larger energy loss due to higher metallic *FF* acting as a mirror for electromagnetic waves. Relative radiation spectra are almost flat for all four samples and minor alteration are caused not because of plasmonic radiation since electric current is needed to excite them [61].

5.4. Radiation of Electrically Excited Plasmonic Emitters

It is clear that a weak plasmonic radiation would be covered by a much stronger BB radiation arising from Joule heating. Cooling the sample to cryogenic temperatures and driving it with pulse wave for measurement in pulse regime is necessary in order to reduce the amount of thermal radiation. Figure 17(a) demonstrates the emission spectra of the sample U11 obtained by changing a method of excitation: starting with an external heating, applying a DC voltage and ending with electrically driving the sample in pulse regime at various *DU* and different temperature. Although the shape of the spectra is quite similar, the intensity of the radiation decreases by more than two orders of magnitude, especially in the frequency range from 50 cm^{-1} to 250 cm^{-1} where the appearance of plasmon emission is expected. Moreover, both the spectra of $DU = 50$ % measured at RT and 110 K temperature shows no significant difference indicating that cooling through cryostat's cold-finger is not sufficient.

The latter fact was additionally examined by measuring the resistance of the sample U11 at different temperatures and various *DU* values and the results are shown in Figure 17(b). It is seen that heating of the sample can be only avoided by driving the samples with short electrical pulses of $DU < 1$ % ($\tau_p < 0.8$ ms).

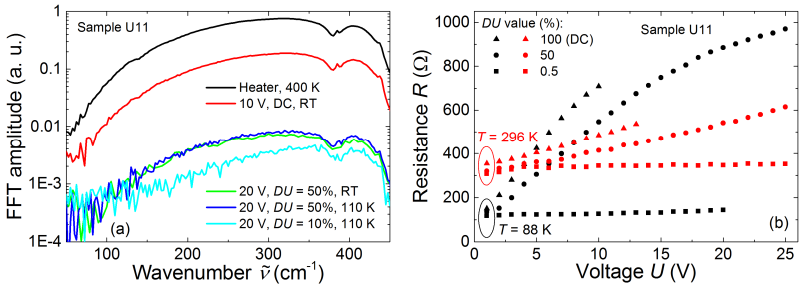

Figure 17. (a) Emission spectra of differently excited sample U11. (b) Resistance of the sample U11 measured at various *DU* values at room and cryogenic temperature.

I-V characteristics of the samples U11 and U6 were measured at temperature $T = 110$ K and are shown in Figure 18(a). Applied EF was calculated by dividing an applied voltage by the length of the sample of $L = 2$ mm. In order to avoid sample heating, small *DU* values up to 2.5 % were used. At low EF the current was independent of *DU* value for the sample U11. The maximum current density of 214 mA/mm was obtained at $E = 500$ V/cm and $DU = 0.5$ %, however, at high EF a decrease of current was observed with increasing *DU* showing a minor heating of the sample. As for the sample U6, the current did not depend on the *DU* value in all the range of EF showing that cooling of the sample U6 was more efficient. However, the absolute current values were smaller as compared to that of the sample U11 due to a larger resistance of the sample U6.

The average THz radiant flux Φ_e was measured by using a calibrated FTIR spectrometer and its dependence on applied electrical power $P_E = UI \cdot DU \equiv UIf\tau_p$ (here U is an applied voltage and I is a current of the sample) is shown in Figure 18(b). The sample U11 showed a non-linear behaviour with a maximum Φ_e value at $P_E \approx 0.55$ W. The latter value corresponds to 2DEG temperature of $T_{ch} \approx (260 \pm 5)$ K that was determined from the measured dependence of the sample's resistance on temperature. As for the sample U6, the $\Phi_e(P_E)$ dependence was steeper as compared to that of the sample U11.

However, it was possible to apply much smaller electrical power P_E due to larger resistance of the sample U6. According to these results further spectral measurements were continued only with the sample U11.

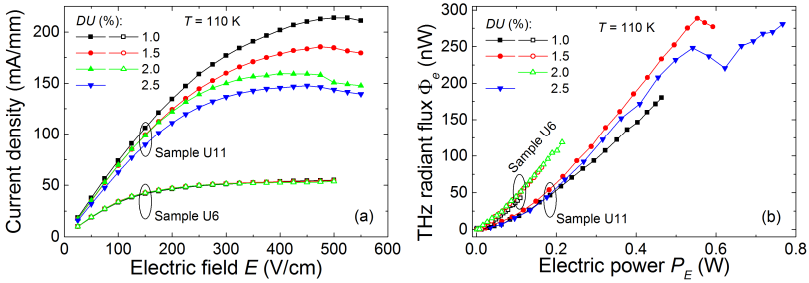

Figure 18. Dependencies of the samples U11 and U6: (a) current density on applied electric field E and (b) radiant flux Φ_e on electrical power P_E. Adapted from [P3] by adding characteristics of the sample U6.

Table 5. Electrical and thermal parameters of the sample U11 pulse spectral measurements when cryostat is cooled down to the temperature of T = 110 K.

U, V	E, V/cm	DU, %	τ_p, ms	I, mA	P_E, W	T_{ch}, K
60	300	5.0	4.0	207	0.62	275
60	300	2.5	20	291	0.44	230
60	300	1.5	1.2	314	0.28	220
60	300	1.0	0.8	341	0.20	205
60	300	0.5	0.4	359	0.11	200
90	450	1.0	0.8	425	0.38	235
40	200	1.5	1.2	301	0.18	130

Electrical parameters used to drive the sample U11 for the THz emission spectral measurements are represented in Table 5. At first, emission spectra of the sample at various DU values from 0.5 % to 5.0 % (τ_p from 0.4 ms to 4.0 ms) were measured and are shown in

Figure 19(a). When $DU < 5$ % an increase of the spectral flux in frequencies above 325 cm^{-1} is due to the thermal BB radiation that develops into continuous spectrum at $DU = 5$ %. This proves the fact that cooling of the sample becomes ineffective with increasing applied electrical power.

Arrows in Figure 19(a) denote frequency of gated and ungated plasmon modes calculated by Equation (1.1). Note that grating of the sample U11 was designed in such a way that the first mode of ungated plasmon has a similar frequency as the second mode of gate plasmon. Since gated plasmons weakly couple with the narrow metal-stripes [62], strengthened interaction of plasmons and increased energy extraction was expected.

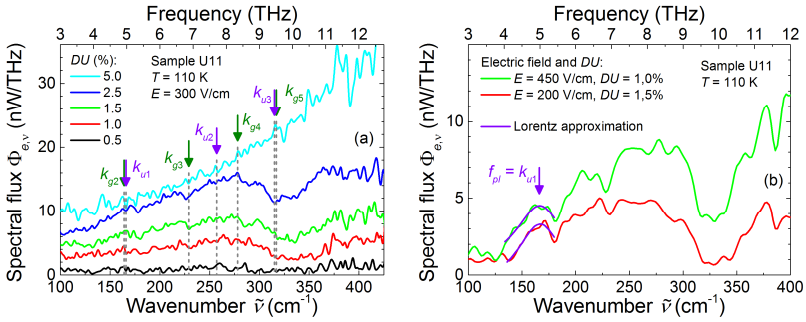

Figure 19. Emission spectra of the sample U11 at $T = 110$ K temperature excited by: (a) various DU values when applied electric field $E = 300$ V/cm (spectra are shifted vertically by 2 nW/THz) and (b) different EF and DU values. Arrows denote frequency of plasmon modes calculated by Equation (1.1) [P3].

Additional emission spectra were measured by changing the voltage of the pulses. The results shown in Figure 19(b) indicate a weak dependence of athermal radiation on the applied EF with different DU value. In specific, when applied EF increases by a factor larger than two, athermal radiation increases only by roughly 20 %. An ungated likely plasmon of frequency $f_{pl} = k_{u1} = 166$ cm^{-1} was

chosen and the peaks in both spectra was fitted by Lorentz function. When $E = 200$ V/cm, full width at half maximum (FWHM) of the peak was of $\Delta f_{pl} = 52.5$ cm^{-1}, while the quality factor was of $Q = f_{pl}/\Delta f_{pl} = 3.2$ and agreed well with the value mentioned in literature [63]. Similar values were obtained when EF was of $E = 450$ V/cm: $\Delta f_{pl} = 55.0$ cm^{-1} and $Q = 3.0$.

Spectrally integrated radiant flux Φ_e of likely plasmon k_{u1} was calculated by integrating the spectra [64]. The values of 6.3 nW and 9.4 nW were obtained for the cases when EF is equal to 200 V/cm and 450 V/cm, respectively. Much higher values of 420 nW and 940 nW, respectively, are obtained if *DU* values are counted in. One of the most important parameters of any emitter is radiant efficiency, calculated as $\eta_e = \Phi_e/P_E$ [64]. Calculated radiant efficiency of ungated likely plasmon was of $35 \cdot 10^{-9}$ and $25 \cdot 10^{-9}$, respectively. Radiant efficiency of likely plasmon was about one tenth as large as radiant efficiency of thermal THz radiation calculated from the data in Figure 18(b) and having a value of about $300\text{-}500 \cdot 10^{-9}$. This shows a potential to increase radiant efficiency by improving the sample's cooling.

With an eye to measuring fundamental mode of a gated plasmon at $k_{g1} = 68$ cm^{-1}, thicker BS were used in order to increase sensitivity of FTIR spectrometer in low frequency region [59]. However, despite an extended frequency range down to 12 cm^{-1}, k_{g1} plasmon mode was still indistinguishable due to aforementioned reason – gated plasmons weakly couple with the narrow metal-stripes [62].

Besides ungated likely plasmon mode at $k_{u1} = 166$ cm^{-1}, spectra in Figure 19 demonstrate more peaks that could be attributed to higher plasmon modes. These peaks are broader and less intensive not only because higher modes couple weakly but also because they are covered by electroluminescence of silicon and oxygen shallow impurities [65]. These impurities are very difficult to avoid, however they can be used as indicators for the investigation of epitaxial layers and as THz emitters [66].

5.5. Chapter Summary

In the fifth chapter of the dissertation the THz radiation from the large-area HEMTs with grating-contact have been investigated. At the beginning, a Fourier spectrometer and the improvements done in order to collect as much signal from the sample as possible were introduced. Then, a theoretical model of radiant spectra which agreed well with the experimental data was introduced. Calibration of spectrometer allowed to recalculate the FFT amplitude from the arbitrary units to the absolute radiant flux units (watt). Next, the grating of the plasmonic emitters was described and supplemented by theoretical values of plasmon modes. Emission spectra of differently excited samples was further analysed in order to understand the most suitable conditions for the plasmonic emission. Finally, the sample was excited by different voltage pulses and the emission spectra measured at cryogenic temperature were compared attributing one of the measured peak to the theoretically calculated value of ungated plasmon.

6. THZ ELECTROLUMINESCENCE FROM SHALLOW IMPURITIES

UID-grown epitaxial AlGaN and GaN layers always contain residual impurities, concentration of which is at least of 10^{15} cm^{-3} [12]. On the one hand, the charge mobility decreases due to these impurities and, at the same time, electronic characteristics deteriorate. However, residual impurities or specially introduced dopants were proposed to be used as radiation centers in solid-state THz radiation sources [66]. In such an emitter, impurities can be excited electrically or optically, and radiation emerges due to electron relaxation from a higher excited states to a ground state. Stimulated emission from the shallow impurities was observed in optically excited Si:P laser [67] while spontaneous electroluminescence – in Ge [68], Si [69] and SiC [70] crystals and in 4-μm-thick GaN epitaxial layers [65], [71]. All of these experiments were carried out at a liquid He temperature ($\leq$ 6 K), because, unlike in conventional pn junction devices, electrons here must not be thermally excited. It was also found that a Si-based THz emitter has a maximum operating temperature of 40 K [69] and a GaN-based – of about 80 K in strong EF [66]. The following section discusses the experimentally observed electroluminescence from the shallow impurities in thin AlGaN/GaN epitaxial layers in the THz-frequency range.

6.1. HEMT Structures on Al_2O_3 Substrate

First of all, the samples U26 and U28 made of TG2196 and TG2219 heterostructures were selected for the electroluminescence measurements. The dimensions of the active area and the ohmic contacts of these samples were the same as of the plasmonic emitters described in Chapter 5. However, the samples U26 and U28 did not have a metal grating on the surface.

Emission spectra were measured at 110 K temperature while driving the samples U26 and U28 by electrical pulses with various *DU*

values from 0.5 % to 2.0 % at a fixed EF of 300 V/cm. The result is shown in Figure 20. Similarly to the spectra shown in Figure 19, emission at frequencies above approx. 325 cm^{-1} is due to thermal BB radiation. The spectra show that the increase of the *DU* value also increases the intensity of BB radiation in both the samples; and the increase in the sample U28 is larger as compared to that of the sample U26. Several peaks arising in low frequency range below 325 cm^{-1} are due to electroluminescence of shallow impurities. The intensity of electroluminescence increases with increasing *DU* value in the sample U26 while the spectrum shape remained almost the same independently of the *DU* value. As for the sample U28, the intensity is decreasing with increasing *DU* value and the shape of the spectra changes as well, showing that cooling of the sample U28 was less efficient as compared with the sample U26. In addition, the alteration of the spectra demonstrates that distribution of electron energy states and electron transition probabilities changes depending on the temperature.

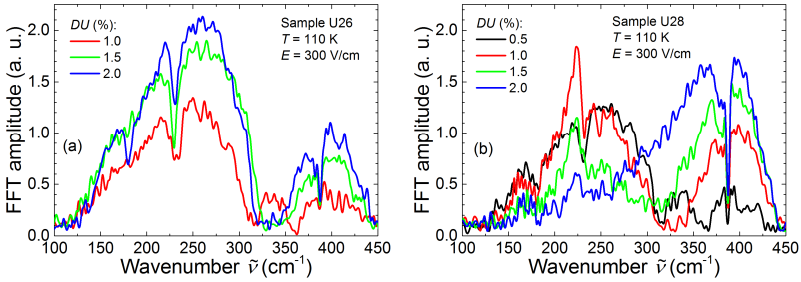

Figure 20. Emission spectra (a) of the sample U26 and (b) of the sample U28 at $T = 110$ K temperature excited by various *DU* values when applied electric field $E = 300$ V/cm [P2].

The dominant shallow donors in epitaxial UID-GaN layers are silicon and oxygen [72], [71]. The most likely electron transition in these impurities are from conduction band to states 2p and 1s (c→2p and c→1s) and between these states (2p→1s).

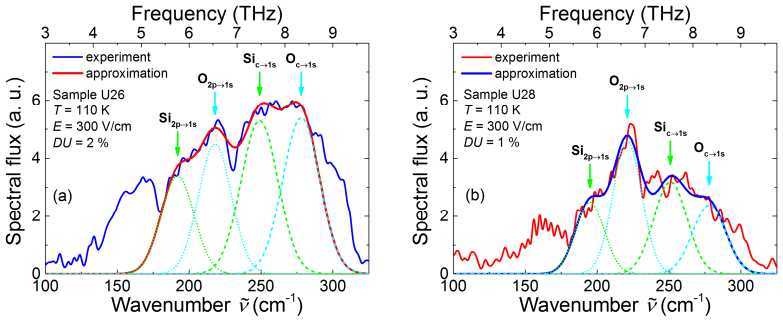

Figure 21. Spectral flux (a) of the sample U26 when $DU = 2.0$ % and (b) of the sample U28 when $DU = 1.0$ %. In both cases applied electric field was of $E = 300$ V/cm and the spectra were measured at $T = 110$ K temperature. Dotted and dashed lines indicate Gaussian function of the 2p→1s and c→1s transitions, respectively, in Si and O shallow impurities. Solid line denotes an envelope of four Gaussian functions. Adapted from [P2] by adding Gaussian functions for the c→1s electron transitions.

Two spectra ($DU = 2.0$ % of the sample U26 and $DU = 1.0$ % of the sample U28) shown in Figure 21 were selected for resolving the energies of electron transitions. Both the spectra had a similar intensity in the frequencies above approx. 325 cm^{-1} in order to minimize the influence of parasitic BB radiation to the interpretation.

Considering a thermal broadening of the states, Gaussian function was chosen to fit the spectral peaks. Starting with the most pronounced peak at approximately 220 cm^{-1} in spectrum of the sample U28, the spectrum was fitted with a fixed FWHM of 27 ± 2 cm^{-1}. Similar procedure was adjusted for the spectrum of the sample U26 yielding a comparable FWHM of 24 ± 2 cm^{-1}. The obtained fitting parameters are given in Table 6.

The peak positions assigned to $Si_{2p\rightarrow1s}$ and $O_{2p\rightarrow1s}$ transitions were very similar in both of the samples. The position of the Si impurity agreed well with the theoretically calculated value (23.5 meV or 189 cm^{-1}) [73] and experimentally measured values (23 meV) in the

epitaxial UID-GaN layer [65] and the GaN substrate [71]. A slight discrepancy was obtained for the O impurity, i.e., divergence from the theoretically calculated value (25.2 meV or 203 cm^{-1}) by 17 cm^{-1} and from the experimentally measured value (26 meV) by 12 cm^{-1}. Results for the c→1s transitions were also tendentious. Obtained position of the Si impurity was about of 250 cm^{-1} and agreed well with the theoretically calculated value (30.8 meV or 248 cm^{-1}), however in case of the O impurity the peak position diverged from the theoretically calculated value (32.4 meV or 261 cm^{-1}) by 17 cm^{-1} [73].

Table 6. The parameters of the Gaussian function used to fit the electroluminescence spectra of the samples U26 and U28. For convenience, the table also contains the parameters of the sample U31 which is described in Section 6.2.

Transition	Impurity	Position cm^{-1}	amplitude a. u.	Ratio of amplitudes	
				Si / O	2p→1s / c→1s
Sample U26					
2p→1s	Si	192 ± 1	3.4 ± 0.2	0.76	Si: 0.64
	O	218 ± 1	4.5 ± 0.1		O: 0.83
c→1s	Si	249 ± 1	5.3 ± 0.2	0.98	
	O	278 ± 1	5.4 ± 0.2		
Sample U28					
2p→1s	Si	195 ± 1	2.5 ± 0.2	0.54	Si: 0.78
	O	221 ± 1	4.6 ± 0.2		O: 1.92
c→1s	Si	251 ± 1	3.2 ± 0.2	1.33	
	O	278 ± 2	2.4 ± 0.2		
Sample U31					
2p→1s	Si	193 ± 1	3.0 ± 0.2	0.91	Si: 0.77
	O	219 ± 2	3.3 ± 0.2		O: 0.73
c→1s	Si	250 ± 2	3.9 ± 0.2	0.87	
	O	280 ± 1	4.5 ± 0.2		

No data was found in literature to explain the increase of the spectral intensity below approx. 180 cm^{-1}, which is clearly seen in Figure 21. Unfortunately, this slope (when $DU < 2$ %) or a broad peak (when $DU = 2$ %) coincides with a position of ungated plasmon f_{pl} shown in Figure 19. Therefore, taking a conservative approach, it cannot be firmly stated that the peak with a corresponding frequency of f_{pl} which was observed in the sample U11 occurs purely due to plasmon radiation.

TG2196 and TG2219 heterostructures were grown in a MOCVD reactor at different pressures of 200 Torr and 100 Torr, respectively. It is known that the carbon concentration is inversely proportional to the growth pressure due to the fact that the removal of methyl radicals from the chamber is faster at higher pressure and/or temperature as well as due to slower supply of TMGa precursor [74]. Therefore two-times larger amount of residual carbon impurities should be expected in the sample U28 which is made of TG2219 heterogeneous. It is also known that the amount of residual oxygen impurities is usually proportional to the amount of carbon impurities due to self-compensation mechanisms [75]. However, it is not known how the change of the technological conditions described above determine the amount of residual silicon impurities in the AlGaN/GaN heterostructures.

6.2. HEMT Structure on SiC Substrate

Analogous investigation of electroluminescence of shallow impurities was also performed with the sample U31 made of HX2688 heterostructure. The design of this sample was identical to that of the samples U26 and U28, however, HX2688 heterostructure was grown on SiC substrate characterized by about ten times higher thermal conductivity as compared to that of the sapphire. Due to the latter reason, no BB radiation above 325 cm^{-1} was observed in the emission spectra of the sample U31 as it is shown in Figure 22(a). Similar fitting

of the spectrum using Gaussian functions with FWHM of 27 ± 2 cm^{-1} (see Figure 22(b)) yielded values of peak position very similar to those of observed in the samples U26 and U28 as indicated in Table 6.

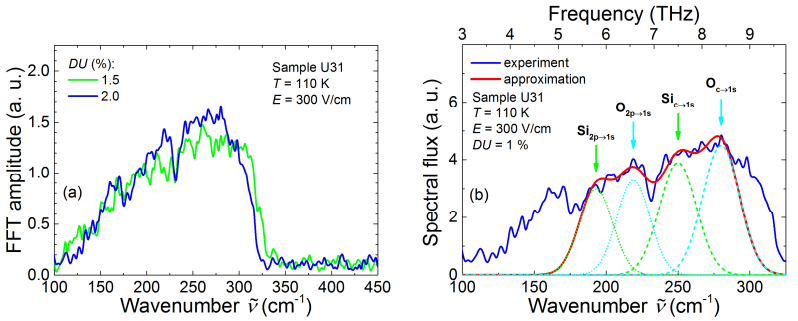

Figure 22. (a) Emission spectra of the sample U31 at T = 110 K temperature excited by various DU values when applied electric field E = 300 V/cm. (b) Spectral flux of the sample U31 when DU = 2.0 %. Dotted and dashed lines indicate Gaussian function of 2p→1s and c→1s transitions, respectively, in Si and O shallow impurities. Solid line denotes an envelope of four Gaussian functions.

It is worth mentioning that, unlike in previously published works, the electroluminescence of shallow impurities was measured at a higher temperature of 110 K and at a weaker EF [66], [65]. A c→2p electron transition was not observed in any of the samples. The energy of this transition, calculated as an energy difference of c→1s and 2p→1s transitions, is about of 7.2 meV or 60 cm^{-1} for Si and O impurities. Even an increased sensitivity of FTIR spectrometer in the lower frequency range by using a thicker BS did not helped to capture c→2p electron transition. It should be noted that the latter transition has not been experimentally observed in the works of other authors [65], [66].

In order to verify the correlation between the growing conditions and the intensity of the electroluminescence of the shallow impurities, the ratios of the fitted Gaussian amplitudes were calculated and are

shown in Table 6. It is seen that the ratio of the Si / O amplitude (0.54) for the 2p→1s transition in the sample U28 is smaller as compared with the same ratio of the sample U26 (0.76). The result coincides with the expected different amount of residual O impurities in the samples U26 and U28 due to different technological conditions during the growth of AlGaN/GaN heterostructures. Unfortunately, this trend does not remain when looking at the ratio of the amplitude for the c→1s transition of the same Si and O impurities, i.e., the ratio of the sample U28 (1.33) is larger as compared with the one of the sample U26 (0.98).

Such contradictory results were determined due to unequal cooling of the samples U26 and U28. By comparing the spectrum of the sample U28 at DU = 0.5 %, with the spectrum at DU = 1 %, one can see that an increase in the duty cycle greatly increases intensity of $O_{2p\rightarrow 1s}$ transition, while intensity of $Si_{2p\rightarrow 1s}$ transition remains almost unchanged. This indicates that the amplitudes of the transition, and, in turn, their ratios is also influenced by the duration of the exciting pulse.

One of the reasons of the discrepancy between the measured peak position and theoretical calculations is the tension occurring during the growth of epitaxial layers. These tensions influence the energy levels of shallow impurities [73]. Another fundamental reason is the influence of other impurities. For example, the theoretically calculated energy for $C_{2p\rightarrow 1s}$ and $C_{c\rightarrow 1s}$ transitions are of 26.8 meV and 34.0 meV (216 cm^{-1} and 274 cm^{-1}). It seems that C shallow impurities fits the experimentally measured spectra even better, however, as mentioned in the previous section, namely O and not C is considered to be one of the main shallow impurities in UID-GaN [71]. Including C or other impurities in the theoretical model, the amplitudes of electron transitions in O and Si would change. At the same time, the ratios of amplitudes would change, which would probably facilitate the interpretation of the results and would make it easier to associate the amplitude of the transition with the growing conditions of heterostructures.

The most accurate answer about the amount of residual impurities could be provided by the secondary ion mass spectroscopy (SIMS) [71], [76]. Unfortunately, the latter test was not performed for the samples described in this work. However, the analysis of electroluminescence spectra presented in this section shows that FTIR spectrometry in the THz range is quite sensitive and therefore can be used to study the shallow impurities. After calibrating the intensity of the electroluminescence peaks of shallow impurities in a sample with known amount of impurities, this method could be used as a complementary tool to SIMS, especially for the investigation of processed AlGaN/GaN heterostructures and manufactured electronic components.

6.3. Chapter Summary

Electroluminescence of shallow impurities has been investigated in the last chapter of the dissertation. Emission spectra of the samples made of various heterostructure grown on different substrates were compared. Peak positions in the measured spectra were compared with theoretical and experimental values obtained by other scientist.

MAIN RESULTS AND CONCLUSIONS

1. The manufacture of designed electronic components (i.e., Schottky diodes and high-electron-mobility transistors) is possible by using a simpler technology. It was shown by experimentally manufacturing AlGaN/GaN samples by a standard UV photolithography that the two-stage technology (i.e., processing of ohmic and Schottky contacts) is sufficient for the rapid and simple production of electronics components. Electrical parameters of such components are comparable to those of commercially available AlGaN/GaN components.
2. By changing the temperature of the rapid thermal annealing process, the optimum temperature for the ohmic contact annealing was determined to be of 830 °C. The investigation of the circular transmission line test structures annealed at the latter temperature yielded the contact resistance of R_c = 1.8 Ω·mm, the specific contact resistivity of $\rho_c = 3.4 \cdot 10^{-5}$ Ω·cm^2, and the transfer length of L_T = 1.9 μm.
3. The leakage current of Schottky diode, measured at a small reverse voltage of -10 V, varied in different samples in a wide range from 0.4 ± 0.1 mA/cm^2 to 3.9 ± 0.5 A/cm^2. It was determined that at low reverse voltage the leakage current depends on the quality of heterostructure surface. Threading dislocation density and surface roughness, which are used to characterize the quality of the surface, correlated well with the leakage currents in Schottky diodes.
4. Investigation of the Schottky diodes at high reverse voltage up to -210 V showed that the leakage current increases due to leakage in the heterostructure volume, most likely at the interface of GaN layer and the substrate, or at the interface of GaN layer and a superlattice if a superlattice is grown in the heterostructure.
5. It was found that despite the higher density of threading dislocations in the samples with superlattice, the breakdown field of Schottky diodes in such samples was higher as compared with

the analogous Schottky diodes made of heterostructures without a superlattice. No damage was found on the surface of the samples that underwent breakdown, so it should be assumed that the breakdown occurred in the volume of the heterostructure.

6. Schottky diodes made of TG2196, TG2219 and HX2688 heterostructures, withstood the highest available reverse voltage of U = -210 V. The minimum value of breakdown electric field was the highest in HX2688 heterostructure and reached more than 420 kV/cm while the leakage current did not exceed 10^2 A/cm^2 in all the applied voltage range.
7. The insertion of AlGaN/GaN superlattice during the growth of heterostructure yields ambiguous results. Higher breakdown field was obtained in Shottky diodes and larger electron mobility was found in high-electron-mobility transistors made of the samples with superlattice. However, an additional conduction channel was formed in the interface of GaN epitaxial layer and the superlattice during the growth of the heterostructure, which caused higher leakage currents at high reverse voltage and a not fully depletable channel of high-electron-mobility transistor channel. In addition, the surface quality of the samples with a superlattice was poorer. These facts indicate that the growing conditions of superlattice were not optimized, which is a prerequisite for achieving the benefits of the superlattice mentioned in literature.
8. The density of two-dimensional electron gas, calculated from the C-V characteristics of the Schottky diode, always yields smaller value than the one determined from the Hall effect measurements due to different states of two-dimensional electron gas during the measurements. However, the electron mobility, calculated using the sheet resistance obtained from the circular transmission line method and the two-dimensional electron gas density obtained from the C-V analysis, is approximately the same as that found from the Hall effect measurements. Therefore, measurements of the C-V characteristics of Schottky diodes and I-V characteristics of circular transmission line test structures are a good alternative

for the determination of two-dimensional electrons gas density if the Hall effect measurement setup is not available.

9. The best parameters of a high-electron-mobility transistor were obtained in the sample made of HX2688 heterostructure and they are as follows: the saturation current I_{DS} = 450 mA/mm, the open-channel resistance R_{ON} = 39 Ω·mm, the leakage current ~10^5 mA/mm, the current ratio of open and closed channel I_{ON}/I_{OFF} = $1.2 \cdot 10^7$, and the transconductance g_m = 170 mS/mm. These were determined by the high-quality of heterostructure layers and the SiC substrate, which has a significantly higher thermal conductivity and a lower lattice mismatch as compared to that of Al_2O_3.
10. A high-electron-mobility transistor without a special THz antenna and a bow-tie type diode based on AlGaN/GaN heterostructure were successfully developed and used to detect the radiation of commercially THz source. The sensitivity and the noise equivalent power values of S = 2.6 V/W and NEP = 0.60 nW/√Hz as well as S = 12 V/W and NEP = 0.45 nW/√Hz, respectively, were obtained. These values are comparable or better than that of InGaAs bow-tie type diodes.
11. It has been shown that off-axis parabolic mirror with the 5-cm-long focal length can accurately determine the position of the metal grating with an area of 2 × 2 mm^2 in respect of a spectrometer. This is of vital importance in order to avoid the influence of peripheral thermal radiation on the measured characteristics.
12. A weak influence of the grating on the emission spectra shape was determined from the measured relative radiation intensity when the samples are excited thermally.
13. In order to reduce heating of the sample, it should be driven by electrical pulses of up to 0.1 W average power having a duration of τ_p = 0.4 ms, a repetition frequency of 12.5 Hz, and a duty cycle of DU = 0.5 % when the sample is made of Al_2O_3-grown AlGaN/GaN heterostructure. If samples are made of analogous

heterostructures grown on a SiC substrate, it is possible to prevent them from heating when they are driven by pulses of up to 0.3 W average power having a duration of τ_p = 1.6 ms, a repetition frequency of 12.5 Hz, and a duty cycle of DU = 2.0%.

14. After examining the change of spectra shape on pulse duration at T = 110 K and fixed pulse frequency, the radiation was found to become continuous due to strong black body radiation when the duty cycle $DU \geq 5.0$ %.
15. The peak of the radiation spectrum of the plasmonic AlGaN/GaN emitter at a frequency of f_{pl} = 166 cm^{-1} was attributed to the first mode of ungated plasmon. The full width of half maximum of the plasmon peak was of Δf_{pl} = 52.5 cm^{-1}, and the quality factor Q = 3.2 was in consistent with the value mentioned in literature. The radiation flux and the radiant efficiency of the plasmon was of Φ_e = 940 nW and $\eta_e = 35 \cdot 10^{-9}$, respectively.
16. Peaks observed in the emission spectra of AlGaN/GaN heterostructures were attributed to the electroluminescence of Si and O shallow impurities occurring due to electron transitions between 2p→1s and c→1s energy levels. After calibrating the amount of residual impurities and the intensity of electroluminescence peaks, THz spectroscopy methods could be used to determine the amount of impurities in AlGaN/GaN HEMT structures.
17. In order to manufacture samples for the investigation of plasmonic radiation in the THz range, it is necessary to consider the influence of the electroluminescence of Si and O shallow impurities in AlGaN/GaN heterostructures.

REFERENCES

[1] V. Tamošiūnas, D. Seliuta, A. Juozapavičius, E. Širmulis, G. Valušis, A. El Fatimy, Y. Meziani, N. Dyakonova, J. Lusakowski, et al., New trends in terahertz electronics, Lith. J. Phys. **46**(2), 131–145 (2006).

[2] S. S. Dhillon, M. S. Vitiello, E. H. Linfield, A. G. Davies, M. C. Hoffmann, J. Booske, C. Paoloni, M. Gensch, P. Weightman, et al., The 2017 terahertz science and technology roadmap, J. Phys. D. Appl. Phys. **50**(4), 043001 (2017).

[3] W. C. Johnson, J. B. Parson, and M. C. Crew, Nitrogen Compounds of Gallium, J. Phys. Chem. **36**(10), 2651–2654 (1931).

[4] The Nobel Prize in Physics 2014, access online, https://www.nobelprize.org/prizes/physics/2014/summary/ (checked on 28th September, 2018).

[5] B. Ozpineci, „Comparison of Wide-Bandgap Semiconductors for Power Electronics Applications“, Oak Ridge, TN, 2004.

[6] B. J. Baliga, Power semiconductor device figure of merit for high-frequency applications, IEEE Electron Device Lett. **10**(10), 455–457 (1989).

[7] E. Johnson, Physical limitations on frequency and power parameters of transistors, IRE Int. Conv. Rec. **13**, (Institute of Electrical and Electronics Engineers, 1966).

[8] H. M. Ng, N. G. Weimann, and A. Chowdhury, GaN nanotip pyramids formed by anisotropic etching, J. Appl. Phys. **94**(1), 650–653 (2003).

[9] I. Gorczyca, N. E. Christensen, E. L. Peltzer y Blancá, and C. O. Rodriguez, Optical phonon modes in GaN and AlN, Phys. Rev. B **51**(17), 11936–11939 (1995).

[10] S. Vassant, F. Pardo, P. Bouchon, F. Marquier, J. J. Greffet, and J. L. Pelouard, Optical control of THz reflectivity with surface waves, Proc. SPIE(September 2011), M. Razeghi, N.

Péré-Laperne, H. O. Everitt, J. M. Zavada, and T. Manzur, Sud., (2011).

[11] K. Motoki, T. Okahisa, N. Matsumoto, M. Matsushima, H. Kimura, H. Kasai, K. Takemoto, K. Uematsu, T. Hirano, et al., Preparation of Large Freestanding GaN Substrates by Hydride Vapor Phase Epitaxy Using GaAs as a Starting Substrate, Jpn. J. Appl. Phys. **40**(Part 2, No. 2B), L140–L143 (2001).

[12] R. Quay, *Gallium Nitride Electronics* (Springer Berlin Heidelberg, Berlin, Heidelberg, 2008).

[13] Y. Cordier, N. Baron, F. Semond, J. Massies, M. Binetti, B. Henninger, M. Besendahl, and T. Zettler, In situ measurements of wafer bending curvature during growth of group-III-nitride layers on silicon by molecular beam epitaxy, J. Cryst. Growth **301**–**302**(SPEC. ISS.), 71–74 (2007).

[14] M. Albrecht, I. P. Nikitina, A. E. Nikolaev, Y. V. Melnik, V. A. Dmitriev, and H. P. Strunk, Dislocation Reduction in AlN and GaN Bulk Crystals Grown by HVPE, Phys. Status Solidi C **176**(1), 453–458 (1999).

[15] X. Q. Shen, H. Matsuhata, and H. Okumura, Reduction of the threading dislocation density in GaN films grown on vicinal sapphire (0001) substrates, Appl. Phys. Lett. **86**(2), 021912 (2005).

[16] H. M. Wang, J. P. Zhang, C. Q. Chen, Q. Fareed, J. W. Yang, and M. A. Khan, AlN/AlGaN superlattices as dislocation filter for low-threading-dislocation thick AlGaN layers on sapphire, Appl. Phys. Lett. **81**(4), 604–606 (2002).

[17] A. Usui, H. Sunakawa, A. Sakai, and A. A. Yamaguchi, Thick GaN Epitaxial Growth with Low Dislocation Density by Hydride Vapor Phase Epitaxy, Jpn. J. Appl. Phys. **36**(Part 2, No. 7B), L899–L902 (1997).

[18] K. H. Kim, J. Li, S. X. Jin, J. Y. Lin, and H. X. Jiang, III-nitride ultraviolet light-emitting diodes with delta doping, Appl. Phys. Lett. **83**(3), 566–568 (2003).

[19] O. Ambacher, J. Smart, J. R. Shealy, N. G. Weimann, K. Chu, M. Murphy, W. J. Schaff, L. F. Eastman, R. Dimitrov, et al., Two-dimensional electron gases induced by spontaneous and piezoelectric polarization charges in N- and Ga-face AlGaN/GaN heterostructures, J. Appl. Phys. **85**(1999), 3222 (1999).

[20] E. T. Yu, G. J. Sullivan, P. M. Asbeck, C. D. Wang, D. Qiao, and S. S. Lau, Measurement of piezoelectrically induced charge in GaN/AlGaN heterostructure field-effect transistors, Appl. Phys. Lett. **71**(19), 2794–2796 (1997).

[21] R. H. Ritchie, Plasma Losses by Fast Electrons in Thin Films, Phys. Rev. **106**(5), 874–881 (1957).

[22] A. V. Chaplik, Absorption and emission of electromagnetic waves by two-dimensional plasmons, Surf. Sci. Rep. **5**(7), 289–335 (1985).

[23] H. Raether, *Excitation of Plasmons and Interband Transitions by Electrons*, Electr. Resist. Thin Met. Film. **88**, G. Hohler, Sud. (Springer-Verlag, Berlin/Heidelberg, 1980).

[24] S. J. Allen, D. C. Tsui, and R. A. Logan, Observation of the Two-Dimensional Plasmon in Silicon Inversion Layers, Phys. Rev. Lett. **38**(17), 980–983 (1977).

[25] V. V. Popov, Plasmon Excitation and Plasmonic Detection of Terahertz Radiation in the Grating-Gate Field-Effect-Transistor Structures, J. Infrared, Millimeter, Terahertz Waves **32**(10), 1178–1191 (2011).

[26] R. A. Höpfel, E. Vass, and E. Gornik, Thermal Excitation of Two-Dimensional Plasma Oscillations, Phys. Rev. Lett. **49**(22), 1667–1671 (1982).

[27] V. V. Popov, A. N. Koudymov, M. Shur, and O. V. Polischuk, Tuning of ungated plasmons by a gate in the field-effect transistor with two-dimensional electron channel, J. Appl. Phys. **104**(2), 024508 (2008).

[28] D. C. Tsui, E. Gornik, and R. A. Logan, Far infrared emission from plasma oscillations of Si inversion layers, Solid State

Commun. **35**(11), 875–877 (1980).

[29] K. Hirakawa, K. Yamanaka, M. Grayson, and D. C. Tsui, Far-infrared emission spectroscopy of hot two-dimensional plasmons in $Al_{0.3}Ga_{0.7}As$/GaAs heterojunctions, Appl. Phys. Lett. **67**(16), 2326 (1995).

[30] T. Otsuji, Y. M. Meziani, T. Nishimura, T. Suemitsu, W. Knap, E. Sano, T. Asano, and V. V Popov, Emission of terahertz radiation from dual grating gate plasmon-resonant emitters fabricated with InGaP/InGaAs/GaAs material systems, J. Phys. Condens. Matter **20**(38), 384206 (2008).

[31] W. Knap, J. Lusakowski, T. Parenty, S. Bollaert, A. Cappy, V. V. Popov, and M. S. Shur, Terahertz emission by plasma waves in 60 nm gate high electron mobility transistors, Appl. Phys. Lett. **84**(13), 2331 (2004).

[32] J. Lusakowski, W. Knap, N. Dyakonova, L. Varani, J. Mateos, T. Gonzalez, Y. Roelens, S. Bollaert, A. Cappy, et al., Voltage tuneable terahertz emission from a ballistic nanometer InGaAs/InAlAs transistor, J. Appl. Phys. **97**(6), 064307 (2005).

[33] A. El Fatimy, N. Dyakonova, Y. Meziani, T. Otsuji, W. Knap, S. Vandenbrouk, K. Madjour, D. Théron, C. Gaquiere, et al., AlGaN/GaN high electron mobility transistors as a voltage-tunable room temperature terahertz sources, J. Appl. Phys. **107**(2), 024504 (2010).

[34] N. Okisu, Y. Sambe, and T. Kobayashi, Far-infrared emission from two-dimensional plasmons in AlGaAs/GaAs heterointerfaces, Appl. Phys. Lett. **48**(12), 776 (1986).

[35] R. Aleksiejūnas, P. Ščajev, S. Nargelas, T. Malinauskas, A. Kadys, and K. Jarašiūnas, Impact of Diffusivity to Carrier Recombination Rate in Nitride Semiconductors: From Bulk GaN to (In,Ga)N Quantum Wells, Jpn. J. Appl. Phys. **52**(8S), 08JK01 (2013).

[36] T. Grinys, R. Dargis, M. Frentrup, A. K. Jucevičienė, K. Badokas, S. Stanionytė, A. Clark, and T. Malinauskas, Facet analysis of truncated pyramid semi-polar GaN grown on

Si(100) with rare-earth oxide interlayer, J. Appl. Phys. **120**(10), 105301 (2016).

[37] R. S. Pengelly, S. M. Wood, J. W. Milligan, S. T. Sheppard, and W. L. Pribble, A review of GaN on SiC high electron-mobility power transistors and MMICs, IEEE Trans. Microw. Theory Tech. **60**(6), 1764–1783 (2012).

[38] M. Chafkin and I. King, How Intel Makes a Chip, access online, https://www.bloomberg.com/news/articles/2016-06-09/how-intel-makes-a-chip (checked on 28th September, 2018).

[39] S. J. Pearton, J. C. Zolper, R. J. Shul, and F. Ren, GaN: Processing, defects, and devices, J. Appl. Phys. **86**(1), 1 (1999).

[40] S. Indrišiūnas, Formation of light harvesting structures for photovoltaics using laser interference ablation (doctoral dissertation, Fizinių ir technologijos mokslų centras, Vilnius, 2018).

[41] G. K. Reeves, Specific contact resistance using a circular transmission line model, Solid. State. Electron. **23**(5), 487–490 (1980).

[42] D. K. Schroder, *Semiconductor Material and Device Characterization*, 3rd leid. (John Wiley & Sons, Inc., Hoboken, NJ, USA, 2005).

[43] P. Kruszewski, P. Prystawko, I. Kasalynas, A. Nowakowska-Siwinska, M. Krysko, J. Plesiewicz, J. Smalc-Koziorowska, R. Dwilinski, M. Zajac, et al., AlGaN/GaN HEMT structures on ammono bulk GaN substrate, Semicond. Sci. Technol. **29**(7), 075004 (2014).

[44] P. Kruszewski, M. Grabowski, P. Prystawko, A. Nowakowska-Siwinska, M. Sarzynski, and M. Leszczynski, Properties of AlGaN/GaN Ni/Au-Schottky diodes on 2°-off silicon carbide substrates, Phys. Status Solidi A **214**(4), 1600376 (2017).

[45] Y. Ni, Z. He, D. Zhou, Y. Yao, F. Yang, G. Zhou, Z. Shen, J. Zhong, Y. Zhen, et al., The influences of AlN/GaN

superlattices buffer on the characteristics of AlGaN/GaN-on-Si (111) template, Superlattices Microstruct. **83**(111), 811–818 (2015).

[46] S. Nakamura, InGaN multiquantum-well-structure laser diodes with GaN-AlGaN modulation-doped strained-layer superlattices, IEEE J. Sel. Top. Quantum Electron. **4**(3), 483–489 (1998).

[47] S. L. Selvaraj, A. Watanabe, A. Wakejima, and T. Egawa, 1.4-kV Breakdown Voltage for AlGaN/GaN High-Electron-Mobility Transistors on Silicon Substrate, IEEE Electron Device Lett. **33**(10), 1375–1377 (2012).

[48] K. Y. Park, B. J. Kwon, Y.-H. Cho, S. A. Lee, and J. H. Son, Growth and characteristics of Ni-based Schottky-type $Al_xGa_{1-x}N$ ultraviolet photodetectors with AlGaN/GaN superlattices, J. Appl. Phys. **98**(12), 124505 (2005).

[49] F. Ren, A. P. Zhang, G. T. Dang, X. A. Cao, H. Cho, S. J. Pearton, J.-I. Chyi, C.-M. Lee, and C.-C. Chuo, Surface and bulk leakage currents in high breakdown GaN rectifiers, Solid. State. Electron. **44**(4), 619–622 (2000).

[50] A. B. Piotrowska, E. A. Kaminska, W. Wojtasiak, W. Gwarek, R. Kucharski, M. Zajac, P. Prystawko, P. Kruszewski, M. Ekielski, et al., Manufacturing Microwave AlGaN/GaN High Electron Mobility Transistors (HEMTs) on Truly Bulk Semi-Insulating GaN Substrates, ECS Trans. **75**(12), 77–84 (2016).

[51] L. Minkevičius, THz vaizdų užrašymo matricos, veikiančios kambario temperatūroje (doctoral dissertation, Fizinių ir technologijos mokslų centras, Vilnius, 2016).

[52] M. Dyakonov and M. Shur, Detection, mixing, and frequency multiplication of terahertz radiation by two-dimensional electronic fluid, IEEE Trans. Electron Devices **43**(3), 380–387 (1996).

[53] S. Ašmontas and A. Sužiedelis, New microwave detector, Int. J. Infrared Millimeter Waves **15**(3), 525–538 (1994).

[54] I. Kašalynas, R. Venckevičius, D. Seliuta, I. Grigelionis, and G. Valušis, InGaAs-based bow-tie diode for spectroscopic terahertz imaging, J. Appl. Phys. **110**(11), 1–6 (2011).

[55] D. Seliuta, E. Širmulis, V. Tamošiūnas, S. Balakauskas, S. Ašmontas, A. Sužiedėlis, J. Gradauskas, G. Valušis, A. Lisauskas, et al., Detection of terahertz/sub-terahertz radiation by asymmetrically-shaped 2DEG layers, Electron. Lett. **40**(10), 631 (2004).

[56] A. El Fatimy, S. Boubanga Tombet, F. Teppe, W. Knap, D. B. Veksler, S. Rumyantsev, M. S. Shur, N. Pala, R. Gaska, et al., Terahertz detection by GaN/AlGaN transistors, Electron. Lett. **42**(23), 1342 (2006).

[57] K. Ikamas, A. Lisauskas, M. Bauer, A. Ramer, S. Massabeau, D. Cibiraite, M. Burakevic, S. Chevtchenko, J. Mangeney, et al., Efficient detection of short-pulse THz radiation with field effect transistors, 2017 Int. Conf. Noise Fluctuations, (IEEE, 2017).

[58] R. Venckevičius, Kompaktiško spektroskopinio THz vaizdinimo sprendimai, naudojant GaAs/AlGaAs ir InGaAs puslaidininkinius nanodarinius (doctoral dissertation, Fizinių ir technologijos mokslų centras, Vilnius, 2016).

[59] P. R. Griffiths and J. A. de Haseth, *Fourier Transform Infrared Spectrometry*, 2nd leid. (John Wiley & Sons, Inc., Hoboken, NJ, USA, 2007).

[60] J. Požela, E. Širmulis, K. Požela, A. Šilėnas, and V. Jucienė, SiC and GaAs emitters as selective terahertz radiation sources, Lith. J. Phys. **53**(3), 163–167 (2013).

[61] M. Dyakonov and M. Shur, Shallow water analogy for a ballistic field effect transistor: New mechanism of plasma wave generation by dc current, Phys. Rev. Lett. **71**(15) (1993).

[62] V. V. Popov, O. V. Polischuk, and M. S. Shur, Resonant excitation of plasma oscillations in a partially gated two-dimensional electron layer, J. Appl. Phys. **98**(3), 033510 (2005).

[63] S. Boubanga-Tombet, F. Teppe, J. Torres, A. El Moutaouakil, D. Coquillat, N. Dyakonova, C. Consejo, P. Arcade, P. Nouvel, et al., Room temperature coherent and voltage tunable terahertz emission from nanometer-sized field effect transistors, Appl. Phys. Lett. **97**(26), 262108 (2010).

[64] A. Žukauskas, *Puslaidininkiniai šviestukai* (Progretus, Vilnius, 2008).

[65] V. A. Shalygin, L. E. Vorobjev, D. A. Firsov, V. Y. Panevin, A. N. Sofronov, G. A. Melentyev, A. V. Antonov, V. I. Gavrilenko, A. V. Andrianov, et al., Impurity breakdown and terahertz luminescence in n-GaN epilayers under external electric field, J. Appl. Phys. **106**(12), 123523 (2009).

[66] V. A. Shalygin, L. E. Vorob'ev, D. A. Firsov, V. Y. Panevin, A. N. Sofronov, G. A. Melentyev, A. V. Andrianov, A. O. Zakhar'in, N. N. Zinov'ev, et al., Emission of terahertz radiation from GaN under impact ionization of donors in an electric field, Bull. Russ. Acad. Sci. Phys. **74**(1), 86–88 (2010).

[67] S. G. Pavlov, R. K. Zhukavin, E. E. Orlova, V. N. Shastin, A. V. Kirsanov, H.-W. Hübers, K. Auen, and H. Riemann, Stimulated Emission from Donor Transitions in Silicon, Phys. Rev. Lett. **84**(22), 5220–5223 (2000).

[68] A. V. Andrianov, A. O. Zakhar'in, I. N. Yassievich, and N. N. Zinov'ev, Terahertz electroluminescence under conditions of shallow acceptor breakdown in germanium, J. Exp. Theor. Phys. Lett. **79**(8), 365–367 (2004).

[69] S. A. Lynch, P. Townsend, G. Matmon, D. J. Paul, M. Bain, H. S. Gamble, J. Zhang, Z. Ikonic, R. W. Kelsall, et al., Temperature dependence of terahertz optical transitions from boron and phosphorus dopant impurities in silicon, Appl. Phys. Lett. **87**(10), 1–4 (2005).

[70] G. Xuan, P. C. Lv, X. Zhang, J. Kolodzey, G. Desalvo, and A. Powell, Silicon carbide terahertz emitting devices, J. Electron. Mater. **37**(5), 726–729 (2008).

[71] W. J. Moore, J. A. Freitas, G. C. B. Braga, R. J. Molnar,

S. K. Lee, K. Y. Lee, and I. J. Song, Identification of Si and O donors in hydride-vapor-phase epitaxial GaN, Appl. Phys. Lett. **79**(16), 2570–2572 (2001).

[72] K. Fujito, S. Kubo, H. Nagaoka, T. Mochizuki, H. Namita, and S. Nagao, Bulk GaN crystals grown by HVPE, J. Cryst. Growth **311**(10), 3011–3014 (2009).

[73] H. Wang and A.-B. Chen, Calculation of shallow donor levels in GaN, J. Appl. Phys. **87**(11), 7859–7863 (2000).

[74] P. B. Klein, S. C. Binari, K. Ikossi, A. E. Wickenden, D. D. Koleske, and R. L. Henry, Current collapse and the role of carbon in AlGaN/GaN high electron mobility transistors grown by metalorganic vapor-phase epitaxy, Appl. Phys. Lett. **79**(21), 3527–3529 (2001).

[75] A. F. Wright, Substitutional and interstitial carbon in wurtzite GaN, J. Appl. Phys. **92**(5), 2575–2585 (2002).

[76] S. J. Pearton, Sud., *Processing of Wide Band Gap Semiconductors* (Noyes Publication / William Andrew Publishing, LLC, Norwich, New York, 2000).

LIST OF PUBLICATIONS RELATED TO THE DISSERTATION

Papers in ISI journals:

[P1] **V. Jakštas**, J. Jorudas, V. Janonis, L. Minkevičius, I. Kašalynas, P. Prystawko, M. Leszczynski, Development of AlGaN/GaN/SiC high-electron-mobility transistors for THz detection, Lith. J. Phys. **58**(2), 188-193 (2018).

[P2] I. Grigelionis, **V. Jakštas**, V. Janonis, I. Kašalynas, P. Prystawko, P. Kruszewski, and M. Leszczyński, Terahertz Electroluminescence of Shallow Impurities in AlGaN/GaN Heterostructures at Temperatures above 80 K, Phys. status solidi **225**, 1700421 (2018).

[P3] **V. Jakštas**, I. Grigelionis, V. Janonis, G. Valušis, I. Kašalynas, G. Seniutinas, S. Juodkazis, P. Prystawko, and M. Leszczyński, Electrically driven terahertz radiation of 2DEG plasmons in AlGaN/GaN structures at 110 K temperature, Appl. Phys. Lett. **110**(20), 202101 (2017).

[P4] **V. Jakštas**, I. Kašalynas, I. Šimkienė, V. Strazdienė, P. Prystawko, M. Leszczynski, Schottky diodes and high electron mobility transistors of 2DEG AlGaN/GaN structures on sapphire substrate, Lith. J. Phys. **54**(4), 227-232 (2014).

Conference proceedings:

[P5] **V. Jakštas**, V. Janonis, R. Venckevičius, L. Minkevičius, G. Valušis, I. Kašalynas, P. Prystawko, A. Nowakowska-Siwinska, and R. Jachymek, Development of the terahertz bow-tie diodes of AlGaN/GaN-heterostructures with high mobility 2DEG, 2017 42nd International Conference on Infrared, Millimeter, and Terahertz Waves (IRMMW-THz), (2017).

[P6] I. Kašalynas, R. Venckevičius, **V. Jakštas**, V. Janonis, J. Laužadis, G. Seniutinas, E. Širmulis, G. Valušis, K. Požela, S. Juodkazis, P. Prystawko, M. Leszczyński, THz emission from grating-coupled AlGaN/GaN heterostructures:

comparison between plasmonic and thermal emission, 2015 40th International Conference on Infrared, Millimeter, and Terahertz Waves (IRMMW-THz), (2015).

[P7] **V. Jakštas**, V. Janonis, A. Bičiūnas, R. Aleksiejūnas, A. Kadys, T. Malinauskas, I. Kašalynas, Impact of a superlattice on electrical properties of AlGaN/GaN/sapphire 2DEG structures, J. Phys. Conf. Ser. **647**, 012055 (2015).

[P8] I. Kašalynas, R. Venckevičius, J. Laužadis, **V. Jakštas**, E. Širmulis, K. Požela, G. Valušis, Efficient THz emission from the grating coupled AlGaN/GaN heterostructure on sapphire substrate, J. Phys. Conf. Ser. **647**, 012005 (2015).

Conference contributions:

[K1] I. Grigelionis, **V. Jakštas**, V. Janonis, I. Kašalynas, G. Seniutinas, S. Juodkazis, P. Prystawko, M. Leszczynski, W. Knap, Electrically driven terahertz emission from plasma oscillations in grating gate of AlGaN/ GaN heterostructures, 12th International Conference on Nitride Semiconductors (ICNS12), Strasbourg, France, 24-28 July, 2017.

[K2] I. Grigelionis, **V. Jakštas**, V. Janonis, I. Kašalynas, P. Prystawko, P. Kruszewski, M. Leszczynski, Terahertz electroluminescence of shallow impurities in AlGaN/GaN heterostructures at temperatures above 80 K, 12th International Conference on Nitride Semiconductors (ICNS12), Strasbourg, France, 24-28 July, 2017.

[K3] **V. Jakštas**, I. Grigelionis, V. Janonis, I. Kašalynas, Terahertz emission from AlGaN/GaN structures with grating-type electrode, 60th International Conference for Students of Physics and Natural Sciences Open readings 2017, Vilnius, Lithuania, 14-17 March 2017.

[K4] **V. Jakštas**, V. Janonis, I. Grigelionis, I. Kašalynas, THz emisijos iš GaN/AlGaN didelio elektronų judrio tranzistorių tyrimas, 6-oji Fizinių ir technologijos mokslų centro

doktorantų ir jaunųjų mokslininkų konferencija (FizTeCh 2016), Vilnius, Lietuva, 2016 m. spalio 26-27 d.

[K5] **V. Jakštas**, V. Janonis, R. Venckevičius, I. Grigelionis, G. Seniutinas, G. Valušis, S. Juodkazis, P. Prystawko, M. Leszczyński, I. Kašalynas, Research on terahertz emission from AlGaN/GaN high electron mobility transistor with grating-type electrodes, Terahertz Emitters, Receivers, and Application VII, SPIE Optics + Photonics 2016, Nanoscience + Engineering, San Diego, USA, 28 August - 1 September, 2016.

[K6] V. Janonis, **V. Jakštas**, I. Grigelionis, I. Kašalynas, Investigation of thermal and plasmonic emission from grating-gated GaN/AlGaN high electron mobility transistors, 45th International School & Conference on the Physics of Semiconductors Jaszowiec 2016, Szczyrk, Poland, 18-24 June 2016.

[K7] I. Kašalynas, **V. Jakštas**, I. Grigelionis, V. Janonis, G. Valušis, G. Seniutinas, S. Juodkazis, P. Prystawko, M. Leszczynski, Terahertz radiation from grating-gated plasmonic AlGaN/GaN HEMT structures, EMN meeting on terahertz: Energy materials nanotechnology, San Sebastian, Spain, 14-18 May 2016.

[K8] V. Janonis, **V. Jakštas**, I. Kašalynas, Investigation of thermal and plasmonic emission from GaN/AlGaN grating gated high electron mobility transistors, 59th Scientific Conference for Students of Physics and Natural Sciences Open Reading 2016, Vilnius, Lithuania, 15-18 March 2016.

[K9] **V. Jakštas**, V. Janonis, I. Kašalynas, Supergardelės įtaka AlGaN/GaN heterostruktūrų elektrinėms savybėms, 5-oji Fizinių ir technologijos mokslų centro doktorantų ir jaunųjų mokslininkų konferencija (FizTeCh 2015), Vilnius, Lietuva, 2015 m. spalio 22-23 d.

[K10] I. Kašalynas, **V. Jakštas**, V. Janonis, J. Laužadis, E. Širmulis, R. Venckevičius, G. Valušis, K. Požela, P. Prystawko,

M. Leszczyński, Investigation of plasmonic and thermal THz emission from grating-coupled AlGaN/GaN high mobility electron transistors, 51st International Conference on Microelectronics, Devices and Materials (MIDEM 2015), Bled, Slovenia), 23-25 September 2015.

[K11] I. Kašalynas, R. Venckevičius, **V. Jakštas**, V. Janonis, J. Laužadis, G. Seniutinas, E. Širmulis, G. Valušis, K. Požela, S. Juodkazis, P. Prystawko, M. Leszczyński, THz emission from grating-coupled AlGaN/GaN heterostructures: comparison between plasmonic and thermal emission, 40th International Conference on Infrared, Millimeter, and Terahertz Waves (IRMMW-THz2015), Hong Kong, 23-28 August 2015.

[K12] **V. Jakštas**, V. Janonis, A. Bičiūnas, R. Aleksiejūnas, A. Kadys, T. Malinauskas, I. Kašalynas, Impact of a superlattice on electrical properties of AlGaN/GaN/sapphire 2DEG structures, 19th International Conference on Electron Dynamics in Semiconductors, Optoelectronics and Nanostructures (EDiSON'19), Salamanca, Spain, 29 June - 2 July 2015.

[K13] I. Kašalynas, R. Venckevičius, J. Laužadis, **V. Jakštas**, E. Širmulis, K. Požela, G. Valušis, Efficient THz emission from the grating coupled AlGaN/GaN heterostructure on sapphire substrate, 19th International Conference on Electron Dynamics in Semiconductors, Optoelectronics and Nanostructures (EDiSON'19), Salamanca, Spain, 29 June - 2 July 2015.

[K14] **V. Jakštas**, V. Janonis, A. Kadys, T. Malinauskas, R. Aleksiejūnas, A. Bičiūnas, I. Kašalynas, Supergardelės įtaka AlGaN/GaN/safyras struktūrų elektrinėms savybėms, 41-oji Lietuvos nacionalinė fizikos konferencija, Vilnius, Lietuva, 2015 m. birželio 17-19 d.

[K15] V. Janonis, **V. Jakštas**, I. Kašalynas, Effect of the superlattice on GaN/AlGaN structures performance via Schottky diode

studies, 58th Scientific Conference for Students of Physics and Natural Sciences Open Reading 2015, Vilnius, Lithuania, 24-27 March 2015.

[K16] J. Laužadis, R. Venckevičius, **V. Jakštas**, I. Kašalynas, THz emission from large AlGaN/GaN HEMTs with grating electrodes, 58th Scientific Conference for Students of Physics and Natural Sciences Open Reading 2015, Vilnius, Lithuania, 24-27 March 2015.

[K17] **V. Jakštas**, V. Janonis, I. Šimkienė, I. Kašalynas, Elektroniniai komponentai, pagaminti iš AlGaN/GaN heterostruktūrų ant safyro padėklo, 4 Fizinių ir technologijos mokslų centro doktorantų ir jaunųjų mokslininkų konferencija (FizTeCh 2014), Vilnius, Lietuva, 2014 m. spalio 28-29 d.

[K18] **V. Jakštas**, R. Venckevičius, I. Šimkienė, I. Kašalynas, P. Prystawko, M. Leszczynski, Development of the electronic devices of AlGaN/GaN HEMT structures grown by MOVPE technique / International Workshop on Nitride Semiconductors (IWN 2014), Wroclaw, Poland, 24-29 August 2014.

ACKNOWLEDGEMENT

First of all, I would like to thank my parents for their love.
I am very thankful for the opportunity to work at the Center for Physical Sciences and technology – the sunsets in the Sunrise Valley are remarkably beautiful.
I am also grateful to dr. Ignas Grigelionis, dr. Linas Minkevičius, and Domas Jokubauskis as well as to other current and previous colleague from the Terahertz photonics laboratory of FTMC for the productive collaboration. It is difficult to overstate my gratitude to prof. Gintaras Valušis for his endless support and optimistic overtones. I am thankful to dr. Arūnas Kadys from VU FF FNI and to dr. Paweł Prystawko from UNIPRESS for the grown heterostructures. I would also like to thank dr. Aoto Takahashi for the valuable discussions on the topic of the dissertation.
I also wish to thank Varlam, who teaches one to enjoy a grain in a pocket as well as a sopka with dwarf-trees. Besides him, Elton and Guy for that fateful Sunday, forcing to look at oneself from the side for many years again and again, Mike for the pipes and a lesson on how important it is to learn to read between the lines, and Diane for the unforgettable things.
Finally, I say thank you to the little ones. And to Julija Grigorjevaitė for cherishing the only value and for the sheep. 人生最大の贈り物は友情であり、私はもう手に入れました。3c33

INFORMATION ABOUT THE AUTHOR

Name, surname	Vytautas Jakštas
Address	Saulėtekio av. 3, LT-10257 Vilnius, Lithuania
E-mail	vytautas.jakstas@ftmc.lt
Education	
2013-2017	PhD studies at the Center for Physical Sciences and Technology.
2010-2012	Master studies at Vilnius University, Faculty of Physics; Degree programme: Materials and technology of optoelectronics.
2006-2010	Bachelor studies Vilnius University, Faculty of Physics ; Degree programme: Computing Physics.
1994-2006	Šiauliai Didždvaris gymnasium
Scientific experience	
Since 2013	Junior researcher, engineer at the Center for Physical Sciences and Technology.
2013	Trainee at Mitsubishi Chemical Group Science and Technology Research Center, Inc (Yokohama, Japan).
2008-2012	Technician, engineer at Vilnius University, Institute of Applied Research.
Since 2008	Lecturer at extracurricular school “Fizikos olimpas”.
Specialization	Photolithography methods; fabrication and characterisation of electronic components; Fourier-transform spectroscopy; analysis of optical, electronic and thermal processes in AlInGaN materials.
Publications	Co-author of 8 ISI papers and 30 conference contributions.

Vilniaus universiteto leidykla
Universiteto g. 1, LT-01513 Vilnius
El. p. info@leidykla.vu.lt,
www.leidykla.vu.lt
Tiražas 23 egz.